

AFRL-IF-RS-TR-2007-53
Final Technical Report
March 2007



HYBRID STEERING SYSTEMS FOR FREE-SPACE QUANTUM COMMUNICATION

Vladimir V. Nikulin

APPROVED FOR PUBLIC RELEASE; DISTRIBUTION UNLIMITED.

STINFO COPY

**AIR FORCE RESEARCH LABORATORY
INFORMATION DIRECTORATE
ROME RESEARCH SITE
ROME, NEW YORK**

NOTICE AND SIGNATURE PAGE

Using Government drawings, specifications, or other data included in this document for any purpose other than Government procurement does not in any way obligate the U.S. Government. The fact that the Government formulated or supplied the drawings, specifications, or other data does not license the holder or any other person or corporation; or convey any rights or permission to manufacture, use, or sell any patented invention that may relate to them.

This report was cleared for public release by the Air Force Research Laboratory Rome Research Site Public Affairs Office and is available to the general public, including foreign nationals. Copies may be obtained from the Defense Technical Information Center (DTIC) (<http://www.dtic.mil>).

AFRL-IF-RS-TR-2007-53 HAS BEEN REVIEWED AND IS APPROVED FOR PUBLICATION IN ACCORDANCE WITH ASSIGNED DISTRIBUTION STATEMENT.

FOR THE DIRECTOR:

/s/

ANNA L. LEMAIRE
Work Unit Manager

/s/

IGOR G. PLONISCH, Chief
Strategic Planning & Business Operations Division
Information Directorate

This report is published in the interest of scientific and technical information exchange, and its publication does not constitute the Government's approval or disapproval of its ideas or findings.

REPORT DOCUMENTATION PAGE				<i>Form Approved</i> OMB No. 0704-0188	
<small>Public reporting burden for this collection of information is estimated to average 1 hour per response, including the time for reviewing instructions, searching data sources, gathering and maintaining the data needed, and completing and reviewing the collection of information. Send comments regarding this burden estimate or any other aspect of this collection of information, including suggestions for reducing this burden to Washington Headquarters Service, Directorate for Information Operations and Reports, 1215 Jefferson Davis Highway, Suite 1204, Arlington, VA 22202-4302, and to the Office of Management and Budget, Paperwork Reduction Project (0704-0188) Washington, DC 20503.</small>					
PLEASE DO NOT RETURN YOUR FORM TO THE ABOVE ADDRESS.					
1. REPORT DATE (DD-MM-YYYY) MAR 2007		2. REPORT TYPE Final		3. DATES COVERED (From - To) Sep 06 – Dec 06	
4. TITLE AND SUBTITLE HYBRID STEERING SYSTEMS FOR FREE-SPACE QUANTUM COMMUNICATION				5a. CONTRACT NUMBER	
				5b. GRANT NUMBER FA8750-06-1-0248	
				5c. PROGRAM ELEMENT NUMBER 62702F	
6. AUTHOR(S) Vladimir V. Nikulin				5d. PROJECT NUMBER 558B	
				5e. TASK NUMBER II	
				5f. WORK UNIT NUMBER RS	
7. PERFORMING ORGANIZATION NAME(S) AND ADDRESS(ES) Vladimir V. Nikulin 1110 Elton Dr. Endicott NY 13760-1407				8. PERFORMING ORGANIZATION REPORT NUMBER	
9. SPONSORING/MONITORING AGENCY NAME(S) AND ADDRESS(ES) AFRL/IFB 26 Electronic Parkway Rome NY 13441-4514				10. SPONSOR/MONITOR'S ACRONYM(S)	
				11. SPONSORING/MONITORING AGENCY REPORT NUMBER AFRL-IF-RS-TR-2007-53	
12. DISTRIBUTION AVAILABILITY STATEMENT APPROVED FOR PUBLIC RELEASE; DISTRIBUTION UNLIMITED. PA# 07-072					
13. SUPPLEMENTARY NOTES					
14. ABSTRACT The proposed research will utilize a mechanical gimbal for extended range of optical connectivity, and a fast beam deflector to create a hybrid beam steering system capable of exercising a very high positioning bandwidth over a full hemisphere of steering angles. System design process will include the solution of such underlying problems as the development of the mechanical and optical subsystems, mathematical description of the hybrid device, optimal task distribution between the mechanical and non-mechanical positioning components, and coordination of the operation of the “coarse” and “fine” system controllers. This work will hybrid two separate technologies using the advantages of each.					
15. SUBJECT TERMS Quantum communication, mechanical gimbal, optical connectivity, hybrid beam steering					
16. SECURITY CLASSIFICATION OF:			17. LIMITATION OF ABSTRACT UL	18. NUMBER OF PAGES 50	19a. NAME OF RESPONSIBLE PERSON Anna L. Lemaire
a. REPORT U	b. ABSTRACT U	c. THIS PAGE U			19b. TELEPHONE NUMBER (Include area code)

TABLE OF CONTENTS

1. INTRODUCTION.....	1
2. GIMBAL DEVICE FOR WIDE-RANGE (COARSE) BEAM STEERING.....	3
2.1. POSE KINEMATICS.....	4
2.1.1. Inverse Pose Kinematics.....	5
2.1.2. Forward pose kinematics	6
2.2. DYNAMICS.....	7
2.3. OVERALL MODEL.....	8
3. ACOUSTO-OPTIC DEVICE FOR AGILE (FINE) BEAM STEERING.....	10
3.1. ACOUSTO-OPTIC DEFLECTION.....	10
3.2.DYNAMICS OF ACOUSTO-OPTIC STEERING.....	12
4. HYBRID BEAM STEERING SYSTEM.....	13
4.1. PROPOSED APPROACH.....	13
4.2. OMNI-WRIST III CONTROL SYSTEM.....	14
4.2.1. Control Synthesis.....	14
4.2.2. System Implementation.....	17
4.3. BRAGG CELL CONTROL SYSTEM	19
4.4. FUSION OF THE TECHNOLOGIES.....	21
4.5. SIMULATION RESULTS	23
5. ADDITIONAL CONSIDERATIONS FOR QUANTUM COMMUNICATION SYSTEMS.....	28
5.1. WAVELENGTH COMPATIBILITY	28
5.2. POLARIZATION COMPATIBILITY	31
6. POLARIZATION CONTROL.....	34
6.1. PLATFORM ATTITUDE ESTIMATION.....	34
6.1.1. Inertial Sensors	34
6.1.2. Quaternions	35
6.1.3. Kalman Filter	37
6.2. SENSOR MOUNT ROLL ANGLE ESTIMATION.....	40
7. CONCLUSIONS	43
REFERENCES	44

LIST OF FIGURES

Figure 2. 1. Omni-Wrist III Sensor Mount	3
Figure 2.2. Omni-Wrist III Kinematic Diagram	4
Figure 2.3. (a) Connection of the Actuator; (b) Azimuth, Declination, Yaw (α), Pitch (β)	4
Figure 2.4. Configuration of the Omni-Wrist Model	8
Figure 3.1. Bragg Cell Operation	11
Figure 3.2. Typical acousto-optic system for two-coordinate beam steering	12
Figure 4.1. Range-bandwidth of a hybrid device	13
Figure 4.2. The hybrid steerer concept	13
Figure 4.3. Decentralized adaptive control system	15
Figure 4.4. Decentralized control system	18
Figure 4.5. Control system configuration	20
Figure 4.6. Hybrid system configuration	21
Figure 4.7. Response of the gimbal control system to a square wave signal applied to the azimuth channel	24
Figure 4.8. Response of the gimbal control system to a square wave signal applied to the elevation channel	24
Figure 4.9. Temporal response of the system to high-frequency jitter without Compensation and with hybrid tracking	25
Figure 4.10. Spectral response of the hybrid steering system	26
Figure 4.11. Response of the hybrid control system to a square wave signal applied to the azimuth channel	26
Figure 4.12. Response of the hybrid control system to a square wave signal applied to the elevation channel	27
Figure 5.1. Intensity distribution for $Q=2\pi$	30
Figure 5.2. Intensity distribution for $Q=4\pi$	31
Figure 5.3. Challenges for maintaining orientation of the polarization state In transmitted signals	32
Figure 5.4. Acousto-optic system utilizing diversity approach to steer A beam with arbitrary polarization	32
Figure 5.5. System for real-time compensation of polarization base distortions	33

1. INTRODUCTION

Quantum communication is a laser communication technology that, in addition to very high data rate and low power requirements of the transmitters, offers unprecedented data security. Optical communication in general is very popular when high security is important because inherently small beam divergence angles facilitate low probability of interception and low probability of detection (LPI/LPD). However, when additional immunity to eavesdropping is required, data encryption may be necessary.

Optical communication offers the unique feature of quantum-based encryption due to the inherent properties of light used as a carrier signal. Current research efforts are aimed at using various quantum states to perform data encoding; however, polarization-based techniques are still the most popular ones for a variety of tasks, including quantum communication (QC), quantum key distribution (QKD), and keyed communication in quantum noise (KCQ).

For many practical needs, quantum communication systems must support operation between mobile platforms, which hinges upon several innovations. In particular, successful pointing, acquisition, and tracking (PAT) require the use of a beacon signal and the capability of accurate and agile alignment of the line-of-sight (LOS) between the communicating terminals performed over a large field of regard. While mechanical devices, such as gimbals, offer relatively slow tracking over a very wide range, they lack in pointing bandwidth necessary for rejecting high frequency vibrations and beam deflection caused by the optical turbulence. In contrast, fast steering and especially non-mechanical devices, such as Bragg cells, enjoy very high bandwidth (on the order of several kHz), but their effective range is very small. Inherent limitations of both gimbals and fast steerers result in shortcomings of the entire PAT system when either of these devices is used as a sole beam steerer. Therefore, focus needs to be shifted to hybrid architectures, exploiting the advantages of the constituting elements.

The proposed research will utilize a mechanical gimbal (such as Omni-Wrist or another commercially available device) for extended range of optical connectivity, and a fast beam deflector to create a hybrid beam steering system capable of exercising a very high positioning bandwidth over a full hemisphere of steering angles. System design process will include the solution of such underlying problems as the development of the mechanical and optical subsystems, mathematical description of the hybrid device, optimal task distribution between the mechanical and non-mechanical positioning components, and coordination of the operation of

the “coarse” and “fine” system controllers. The efficiency of the developed system under various operational conditions will be investigated and compared against known designs. It is proposed to develop advanced control strategies that would assure a highly coordinated operation of both system components, thus resulting in a beam steerer with previously unknown range, agility and accuracy.

2. GIMBAL DEVICE FOR WIDE-RANGE (COARSE) BEAM STEERING

Omni-Wrist III (see Fig. 2.1) is proposed as a possible device for coarse steering. It is a new sensor mount developed under Air Force funding that emulates the kinematics of a human wrist. Driven by two linear motors and computer controlled, it is capable of a full 180° hemisphere of pitch/yaw motion. A comprehensive laboratory testing of one of few existing devices of this type, installed in the Laser Communications Research Laboratory at Binghamton University, has resulted in the establishment of a complete transfer matrix-type model relating pitch/yaw coordinates of the sensor mount to the motor encoder signals.

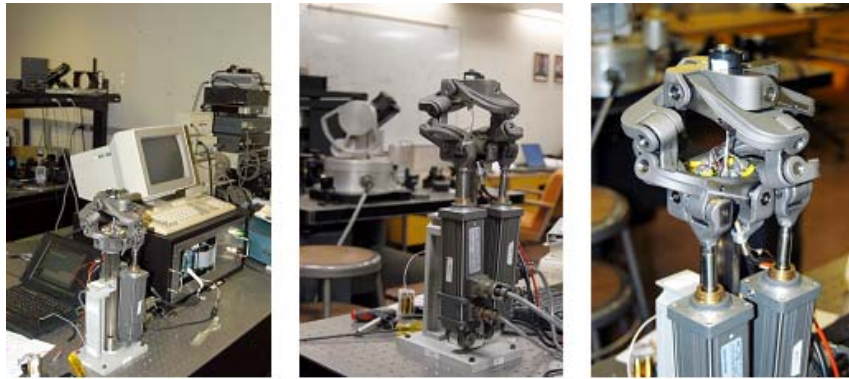


Figure 2.1. Omni-Wrist III Sensor Mount

In contrast to traditional robotic manipulators, the actuators driving Omni-Wrist III are not located in the joints but rather attached to the links, mimicking the attachment of muscles to bones in biological structures. The resultant device is a two-degree-of-freedom system capable of a full 180° hemisphere of singularity-free yaw/pitch motion with up to 5 lbs of payload. In comparison to traditional gimbals positioning devices, Omni-Wrist III enjoys increased bandwidth due to a greater power/mass ratio, and reduced inertia and friction. However, its mechanical design does not eliminate nonlinearities and cross-coupling, complicating the controls task. In our previous work we developed the solution to the inverse and forward pose kinematics problem, and investigated the dynamics of the system, as outlined in the following sections of this chapter. The resulting mathematical model of Omni-Wrist III builds a framework for the synthesis of advanced control strategies required to utilize this device to its full potential.

2.1. POSE KINEMATICS.

The cross-shaped moving sensor mount is connected to the stationary platform of the same shape through four identical legs, each comprising three links and four revolute joints. Two of the legs are redundant for the development of the pose kinematics and are omitted in the kinematic diagram (see Fig. 2.2). The position and orientation of the joints is symbolized by short thick lines. The linear motors are connected to the two bottom links as shown in Fig. 2.3(a).

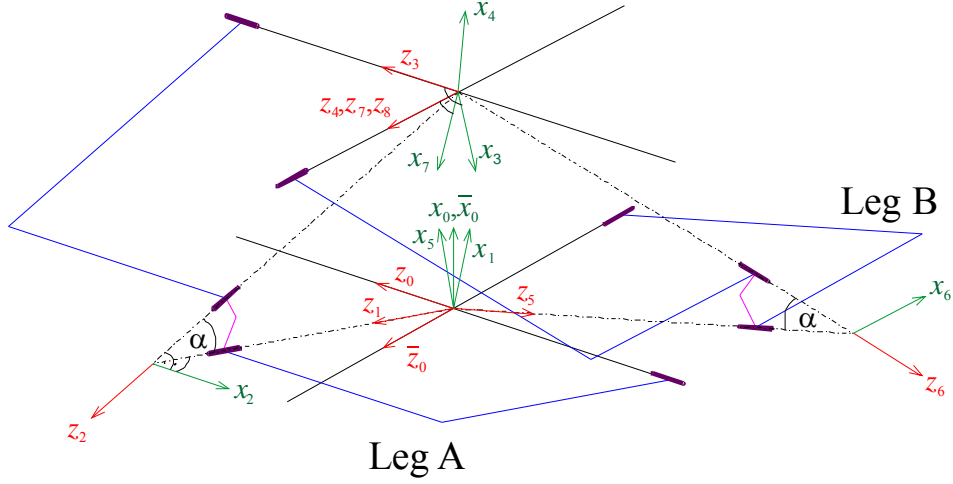


Figure 2.2. Omni-Wrist III Kinematic Diagram

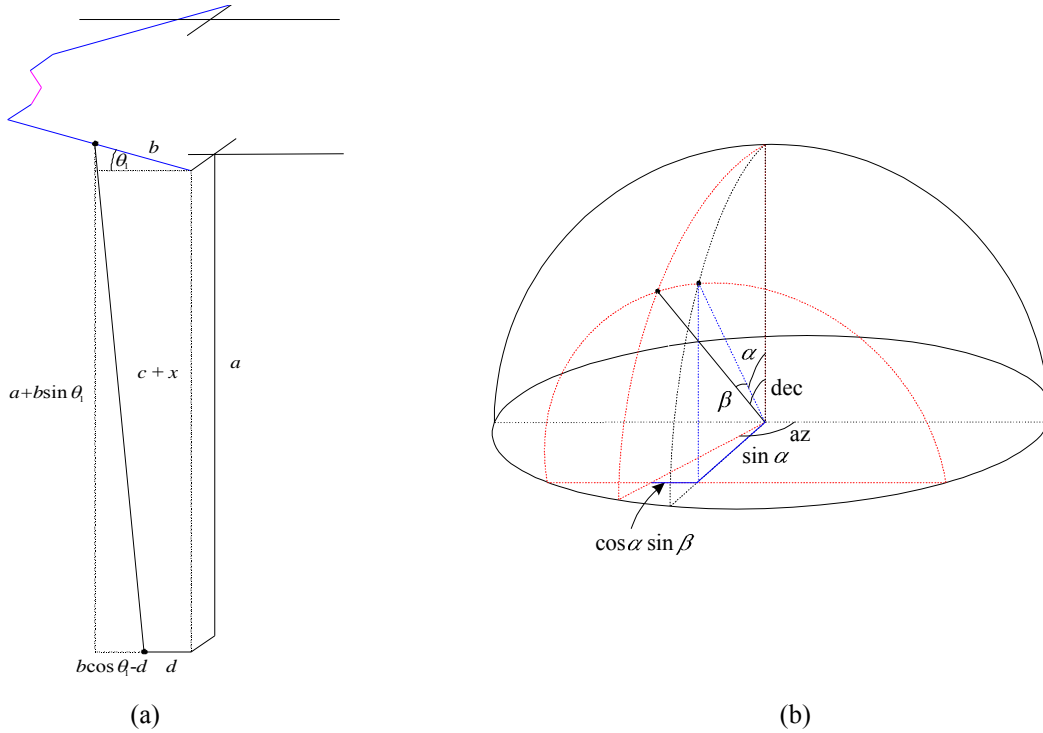


Figure 2.3. (a) Connection of the Actuator; (b) Azimuth, Declination, Yaw (α), Pitch (β)

In the three-step process of finding the pose kinematics solutions, the correspondence between the azimuth and declination and yaw and pitch coordinates is found, as well as between angles θ_1 through θ_8 and the yaw and pitch angles and between the angles θ_1 and θ_5 describing the rotation of the joints connecting Leg A and Leg B to the stationary platform and the position of the actuators. The structure of Omni-Wrist III is captured in the kinematic diagram in Fig. 2.2 showing the x and z axes of all intermediate coordinate frames defined according to [1]. The corresponding Denavit-Hartenberg parameters could be found to derive the transformation between the stationary frame and the sensor mount frame through Leg A and Leg B [2]. Both transformations are equal to the transformation into the yaw, pitch and roll coordinate system:

$$A_1 \times A_2 \times A_3 \times A_4 = B_0 \times B_1 \times B_2 \times B_3 \times B_4 = C, \quad (2.1)$$

where C is defined as

$$C = \begin{bmatrix} C_a C_o & C_a S_o S_n - S_a C_n & C_a S_o C_n + S_a S_n & x \\ S_a C_o & S_a S_o S_n + C_a C_n & S_a S_o C_n - C_a S_n & y \\ -S_o & C_o S_n & C_o C_n & z \\ 0 & 0 & 0 & 1 \end{bmatrix}, \quad (2.2)$$

where indexes n , o and a correspond to the roll, yaw and pitch coordinates, and S and C denote a sine and a cosine, respectively.

2.1.1. Inverse Pose Kinematics. For the solution to the inverse pose problem, the actuator encoder values need to be found, which correspond to the given azimuth and declination coordinates. This is achieved in three steps. First, the yaw and pitch coordinates are found, which correspond to the azimuth and declination coordinates, followed by determining the values of the eight joint variables (angles θ_1 through θ_8) corresponding to the yaw and pitch coordinates. In the last step, the correspondence between the actuator encoder values and the values of θ_1 and θ_5 (parameters of joints between the bottom links and the stationary platform) is established.

The solution to the first step can be found by investigating Fig. 2.3 (b), which shows the graphical representation of these equations:

$$\cos^2(yaw) = \frac{1 + \tan^2(az) \cos^2(dec)}{1 + \tan^2(az)} \quad (2.3)$$

$$\cos(pitch) = \frac{\cos(dec)}{\cos(yaw)}. \quad (2.4)$$

Application of the second step is explained in detail in [2], and it results in the following relationships between two pairs of variables in each leg:

$$\begin{aligned}\theta_2 &= \theta_3 + \pi \\ \theta_4 &= -\theta_1\end{aligned}\tag{2.5}$$

for leg A and

$$\begin{aligned}\theta_6 &= \theta_7 + \pi \\ \theta_8 &= -\theta_5\end{aligned}\tag{2.6}$$

for leg B, simplifying significantly the analytic solution for the remaining variables.

The key to the last step of the solution to the inverse kinematic problem, the connection of the actuators, lies in Fig. 2.3(a), which shows a geometric model of the situation. The corresponding equations, which provide values for Ax_1 and Ax_2 , the actuator encoder positions, from θ_1 and θ_5 are

$$\begin{aligned}(a + b \sin \theta_1)^2 + (b \cos \theta_1 - d)^2 &= (c + Ax_1)^2, \\ (a + b \sin \theta_5)^2 + (b \cos \theta_5 - d)^2 &= (c + Ax_2)^2,\end{aligned}\tag{2.7}$$

where c represents the extension of the actuator corresponding to encoder value of zero. The model implemented in the computer controller supplied with the Omni-Wrist III but without documentation was used as a black box to provide data for the determination of a , b , c , and d utilizing genetic optimization [2], [3].

2.1.2. Forward pose kinematics. Similarly to the inverse kinematics case, the forward pose problem is solved in three steps, now in reversed order. At first, angles θ_1 and θ_5 are determined from the knowledge of the actuator encoder values Ax_1 and Ax_2 . Then, the remaining angles θ_2 through θ_4 , θ_6 through θ_8 and the yaw and pitch are derived from angles θ_1 and θ_2 followed by the conversion of the yaw/pitch coordinates into azimuth and declination. In the first step, the quadratic terms in (2.7) are expanded to

$$\begin{aligned}a^2 + b^2 + d^2 - (c + Ax_1)^2 + 2ab \sin(\theta_1) &= 2bd \cos(\theta_1), \\ a^2 + b^2 + d^2 - (c + Ax_2)^2 + 2ab \sin(\theta_5) &= 2bd \cos(\theta_5).\end{aligned}\tag{2.8}$$

Squaring (2.8) and rearranging produces

$$\begin{aligned}\sin^2 \theta_1 4b^2 (a^2 + d^2) + \sin \theta_1 4ab (a^2 + b^2 + d^2 - (c + Ax_1)^2) + (a^2 + b^2 + d^2 - (c + Ax_1)^2)^2 - 4b^2 d^2 &= 0, \\ \sin^2 \theta_5 4b^2 (a^2 + d^2) + \sin \theta_5 4ab (a^2 + b^2 + d^2 - (c + Ax_2)^2) + (a^2 + b^2 + d^2 - (c + Ax_2)^2)^2 - 4b^2 d^2 &= 0,\end{aligned}\tag{2.9}$$

which are simple quadratic equations and can be easily solved to give θ_1 and θ_5 .

In the next step, S_2 is expressed from element of the transformation matrices in [2] as

$$S_2 = \frac{S_1 - S_5}{C_1} \frac{1 - C_\alpha}{S_\alpha} + \frac{C_5}{C_1} S_6 \quad (2.10)$$

and manipulated further to produce [2]

$$C_1 \frac{1 - C_\alpha}{S_\alpha} + \frac{S_1}{C_1} (S_1 - S_5) \frac{1 - C_\alpha}{S_\alpha} + \frac{S_1}{C_1} C_5 S_6 = C_6. \quad (2.11)$$

Squaring and rearranging (2.11) forms

$$C_6^2 \left(1 + \left(\frac{S_1}{C_1} C_5 \right)^2 \right) + 2C_6 \left(C_1 + \frac{S_1}{C_1} (S_1 - S_5) \right) \frac{1 - C_\alpha}{S_\alpha} - \left(\frac{S_1}{C_1} C_5 \right)^2 + \left[\left(C_1 + \frac{S_1}{C_1} (S_1 - S_5) \right) \frac{1 - C_\alpha}{S_\alpha} \right]^2 = 0, \quad (2.12)$$

which can easily be solved to obtain θ_6 . In an equivalent procedure, S_6 can be expressed from element of the transformation matrices to produce [2]

$$C_5 \frac{1 - C_\alpha}{S_\alpha} + \frac{S_5}{C_5} (S_5 - S_1) \frac{1 - C_\alpha}{S_\alpha} + \frac{S_5}{C_5} C_1 S_2 = -C_2, \quad (2.13)$$

which can be squared and rearranged to form

$$C_2^2 \left(1 + \frac{S_5}{C_5} C_1 \right)^2 + 2C_2 \left(C_5 + \frac{S_5}{C_5} (S_5 - S_1) \right) \frac{1 - C_\alpha}{S_\alpha} - \left(\frac{S_5}{C_5} C_1 \right)^2 + \left[\left(C_5 + \frac{S_5}{C_5} (S_5 - S_1) \right) \frac{1 - C_\alpha}{S_\alpha} \right]^2 = 0 \quad (2.14)$$

to obtain θ_2 .

In a similar fashion, the yaw and pitch coordinates θ_o and θ_a can be obtained as follows

$$\begin{aligned} S_1 C_4 (C_2 C_3 - S_2 S_3 C_\alpha) - (C_1 S_3 C_4 - S_1 S_2 S_4) S_\alpha - C_1 S_4 C_\alpha &= S_a C_o \\ C_4 (S_2 C_3 + C_2 S_3 C_\alpha) - C_2 S_4 S_\alpha &= -S_o \end{aligned} \quad (2.15)$$

and converted into azimuth and declination by using the following equations, which are represented graphically in Fig. 2.3(b)

$$\begin{aligned} \cos(dec) &= \cos(yaw) \cos(pitch) \\ \tan(az) &= \frac{\sin(yaw)}{\cos(yaw) \sin(pitch)}. \end{aligned} \quad (2.16)$$

2.2. DYNAMICS.

Due to the necessity for a successful development of a control system, the dynamic properties of the Omni-Wrist were also investigated. Because of the complicated structure of the device, a response was collected at thirteen different points on the hemisphere covered by Omni-Wrist III, with azimuth and declination values of (0,0), (0,30), (60,30), (120,30), (180,30), (240,30), (300,30), (0,60), (60,60), (120,60), (180,60), (240,60), and (300,60). The actuators

exhibited the velocity response of a first order system; therefore a least squares estimation procedure was implemented to fit the response of a first order system to the response of the Omni-Wrist in the form

$$G(s) = \frac{k}{s+a} . \quad (2.17)$$

The results of the estimation are summarized in [2] and [3], where the placement of poles at the thirteen different locations for axis 1 and axis 2 in positive and negative direction were found. All poles are located in the 95% confidence interval around 47 for the positive direction and 25 for the negative direction for both axes.

While the magnitude of the response differs in the positive and negative direction, it is possible to model the dynamics of the system using only two transfer functions for each actuator with voltage input and position output as

$$G_1^+(s) = \frac{2.3 \cdot 10^6}{s^2 + 47s}, \quad G_1^-(s) = \frac{2.4 \cdot 10^6}{s^2 + 25s}, \quad G_2^+(s) = \frac{1.7 \cdot 10^6}{s^2 + 47s}, \quad G_2^-(s) = \frac{1.9 \cdot 10^6}{s^2 + 25s} . \quad (2.18)$$

2.3. OVERALL MODEL.

The developed mathematical model is a crucial starting point for the design of an efficient control system. Fig. 2.4 represents the proposed configuration of the mathematical model of Omni-Wrist that comprises two modules:

DYNAMICS represents the dynamics of two independently operating linear actuators coupled to the sensor mount through a series of links and joints. It includes two transfer functions, $G_1(s)$ and $G_2(s)$, describing the typical linear relationships between the control efforts, voltages U_1 and U_2 , and the resultant linear displacements, x and y .

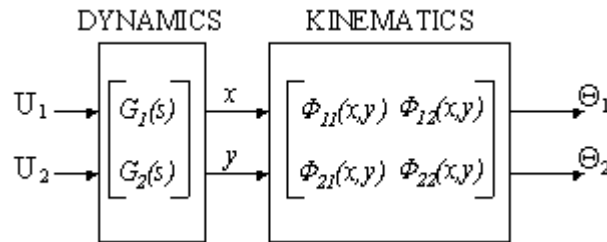


Figure 2.4. Configuration of the Omni-Wrist model

KINEMATICS describes the nonlinear static relationship between the linear actuator displacements, x and y , and the angular displacements of the platform, Θ_1 and Θ_2 . Elements $\Phi_{ij}(x,y)$, $i,j=1,2$, reflect the complex kinematics of the Omni-Wrist structure. Analysis of the system has resulted in a system of trigonometric equations; however, these equations are too

complex for any direct use, and it seems to be more practical to represent both the kinematics and inverse kinematics of the device by a sequence of three transformations [2]. Development of this module implies the solution of the direct pose kinematics problem utilizing the Denavit-Hartenberg approach and finding transformation of the linear encoder readings into joint coordinates, then into the yaw, pitch and roll angles, and finally into the azimuth and declination coordinates.

3. ACOUSTO-OPTIC DEVICE FOR AGILE (FINE) BEAM STEERING

In order to transition the technology being developed under various quantum communication R&D initiatives to military and commercial end users, several outstanding problems must be solved. Among these is the development of agile, compact beam steering. This is a requirement for Air Force applications where optical communications gear must be fitted to an airframe, which places severe demands on the pointing and tracking element.

The state of the art in beam steering employs gimbals for coarse steering augmented by fast steering mirrors (FSM) for fine steering. However, the current-generation mirrors are barely adequate for airborne applications. In spite of their simplicity and well established usage of tip-tilt FSM as a fine steering device, they have a few well known drawbacks: relatively high total weight, their actuators require fairly large currents and consequently high plug-wall power of the electrical drivers. Inertia and mirror's eigenmode interaction typically limit their bandwidth to less than 1 kHz, while it is commonly known in atmospheric laser beam propagation that adaptive systems faster than 1 kHz are highly desirable to overcome optical turbulence induced by the airframe's skin and bow shock flows. Development of a practical system demands a replacement for the FSM that is small, light, low power, and capable of improving the control bandwidth by a factor of 4 or more.

Acousto-optics deflection (AOD) technology can offer much larger bandwidth (more than 20 kHz) within roughly the same excursion range. We believe that a system can be developed that is substantially smaller and lighter than the FSMs, that requires almost an order of magnitude less power, and that can achieve control bandwidths of several kHz. As a practical example, latest models of handheld barcode scanners are increasingly employing miniature AOD elements, particularly for scanning of fast moving objects.

3.1. ACOUSTO-OPTIC DEFLECTION.

An acousto-optic cell utilizes the effect of Bragg diffraction of the laser beam incident upon a volume grating (see Fig. 3.1). An ultrasonic wave is used to create regions of expansion and compression inside the Bragg cell, causing changes in density. The index of refraction is then periodically modulated and the medium becomes equivalent to a moving phase grating [4]

$$\Delta n(z,t) = \Delta n \sin(w_s t - k_s z), \quad (3.1)$$

where: z is the position inside the Bragg cell along the vertical axis; w_s and k_s = acoustic frequency and wave number, respectively.

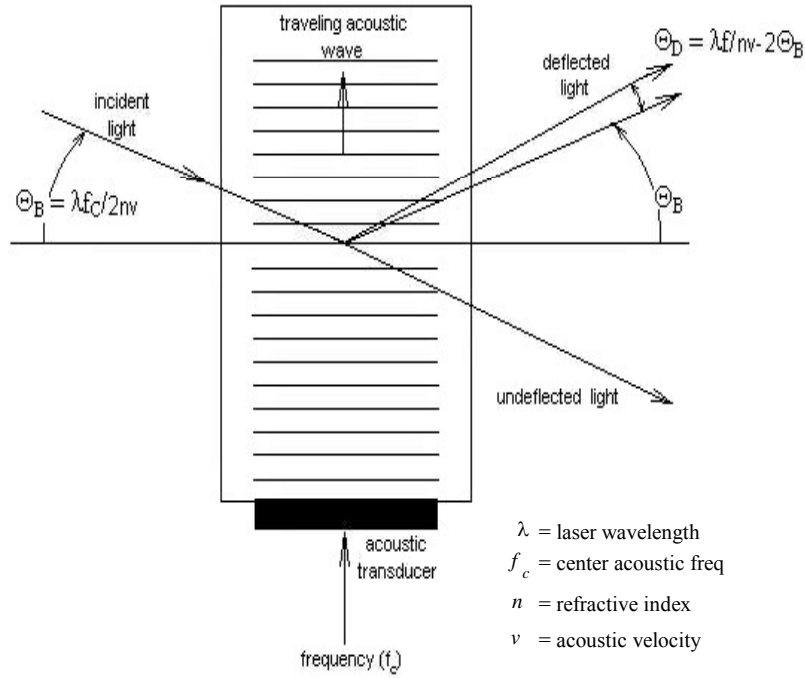


Figure 3.1. Bragg cell operation

The angle of incidence is selected in such fashion that the conservation of energy and the principle of momentum conservation between the acoustic and optical wave vectors during light-sound interaction is preserved [5]. It leads to a mathematical expression commonly known as the Bragg angle

$$\Theta_B = \sin^{-1}(\lambda f_c / 2nv), \quad (3.2)$$

When the acoustic frequency applied to the Bragg cell is varied from f_c to $(f_c + \Delta f_s)$, there is a change in the magnitude of the sound vector equal to $\Delta K = 2\pi(\Delta f_s)/v$. As a result, the diffracted beam will propagate along the direction that least violates the momentum conservation principle. This change in the sound vector results in a small angular motion of the deflected beam and is found to be proportional to the frequency of the input acoustic signal via

$$\Delta\Theta = (\lambda * \Delta f_s) / (n * v), \quad (3.3)$$

Hence the direction of the diffracted beam could be controlled by the frequency of the acoustic wave f , with a deflection angle

$$\theta_D = \lambda / (nv) * (f - f_c) \quad (3.4)$$

A closed-loop configuration of an acousto-optic system with two Bragg cells is shown in Fig.3.2.

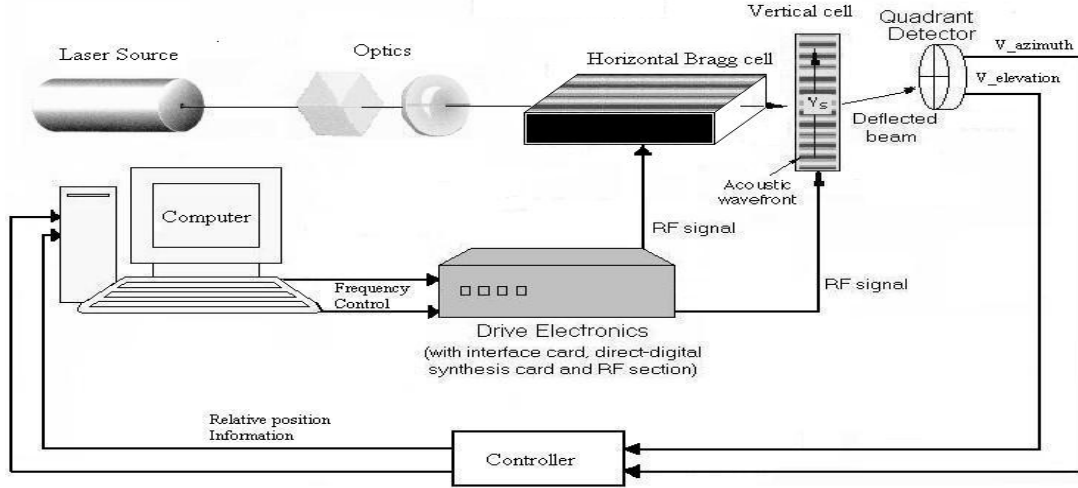


Figure 3.2. Typical acousto-optic system for two-coordinate beam steering

3.2.DYNAMICS OF ACOUSTO-OPTIC STEERING.

The deflection model (3.2) suggested as a result of theoretical study of the acousto-optic phenomena uses the acoustic frequency of the transducer as an input and deflection angle of the laser beam as an output; however, this equation does not reflect any transient when steering is performed. Bragg cells are characterized by very fast beam steering, and the following dynamic changes describe the process. The deflection angle θ_D changes while the acoustic wave traverses the laser beam that has width w . Therefore, response time is determined by the ratio of the Bragg cell aperture to the acoustic velocity in the interaction media. A typical value for tellurium dioxide lies in the 10-100 μ s range; however, advanced controls are still required for proper operation of the beam steering system, especially in the presence of platform vibrations or strong atmospheric turbulence. Since the deflection angle does not experience any overshoot [6], dynamics of this process can be best described by a first order system (lag filter). As a result, the model of the Bragg cell can be established in the form of the following transfer function [7]

$$G(s) = \theta_D / (f - f_c) = [\lambda / (nv)] * [w_b / (s + w_b)] \quad (3.5)$$

where w_b is a parameter of the lag filter modeling access time of the Bragg cell.

Definition of the parameters of the above model and extensive study of the acousto-optic phenomena suggests no cross-coupling between two sequentially mounted Bragg cells, when two-dimensional steering is required.

4. HYBRID BEAM STEERING SYSTEM

As outlined in the previous chapters, state-of-the-art beam steering devices cannot offer adequate combination of features to satisfy the range and speed requirements imposed by application of lasers in mobile communication systems. Hence, the pointing, acquisition, and tracking (PAT) task of any laser-based, and particularly, quantum communication system is superficially decomposed into the “slow-high-magnitude motion” problem, known as coarse steering, and the “fast-low-magnitude motion”, known as fast steering. This research is focused on the development of a hybrid system addressing the needs of the entire PAT task, utilizing two different advanced beam steering technologies fused together by hierarchical control. The first technology is the Omni-Wrist III mechanical system known for its superior dynamics, in comparison with traditional gimbals, and a full hemisphere steering range [2]. The second technology is the acousto-optic Bragg cell, virtually inertia-less but with a very limited steering range [8], [9].

4.1. PROPOSED APPROACH.

Fig. 4.1 illustrates graphically the idea of wide range connectivity facilitated by a mechanical device (such as the Omni-Wrist gimbal) combined with high bandwidth of a narrow-range agile steerer (Bragg cell). As a configuration example, two Bragg cells, required to provide two-coordinate beam deflection, could be integrated into an optical setup and placed

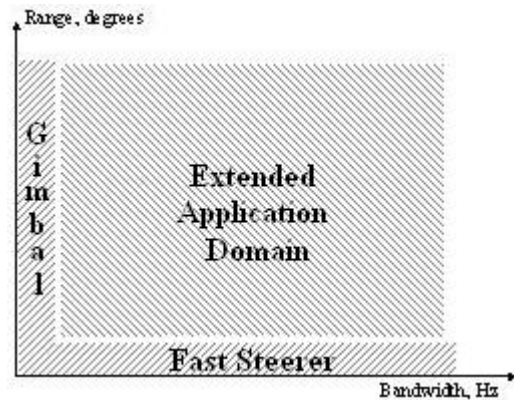


Figure 4.1. Range-bandwidth of a hybrid device directly on the sensor mount of the Omni-Wrist, as illustrated in Fig. 4.2. One of the most attractive features of the proposed system is its ability to effectively cover a wide area in the “range - bandwidth” domain in the sense that the high bandwidth capability could be “delivered” to any location on the hemisphere of system

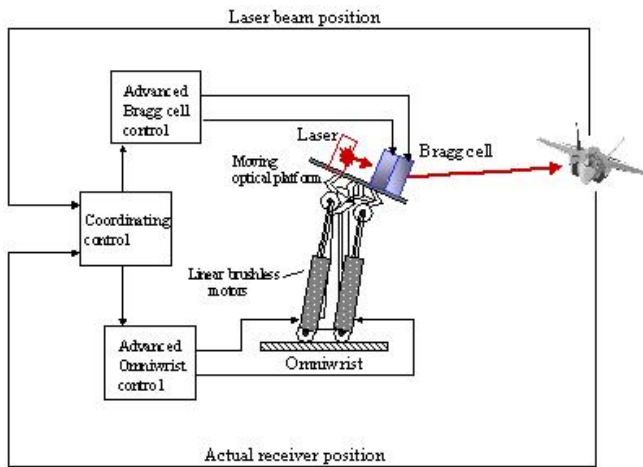


Figure 4.2. The hybrid steerer concept

operation (it should be realized that high frequency components of any steering task have small amplitudes).

4.2. OMNI-WRIST III CONTROL SYSTEM.

4.2.1. Control Synthesis. When used as a steering device for pointing, acquisition, and tracking (PAT), Omni-Wrist III could be viewed as a two-input-two-output system that positions the laser beam over a wide range of azimuth and declination angles. Its model, with the structure shown in Fig.2.4, could be presented with a single nonlinear transformation that accounts for both kinematic and dynamic properties as follows.

$$\begin{bmatrix} \Theta_1 \\ \Theta_2 \end{bmatrix} = \begin{bmatrix} \Theta_{11}(x, y) & \Theta_{12}(x, y) \\ \Theta_{21}(x, y) & \Theta_{22}(x, y) \end{bmatrix} \begin{bmatrix} G_1(s) & 0 \\ 0 & G_2(s) \end{bmatrix} \begin{bmatrix} U_1 \\ U_2 \end{bmatrix} = \begin{bmatrix} g_{11}(s, x, y) & g_{12}(s, x, y) \\ g_{21}(s, x, y) & g_{22}(s, x, y) \end{bmatrix} \begin{bmatrix} U_1 \\ U_2 \end{bmatrix} \quad (4.1)$$

Hence, the output of either dynamic channel (azimuth or declination) can be found as

$$\Theta_i = g_{ii}U_i + g_{ij}U_j \quad (4.2)$$

Let \bar{d}_i (disturbance signal) represent cross-coupling effects, nonlinearities and other unmodeled dynamics [10], such that (4.2) becomes

$$\Theta_i = G_i U_i + \bar{d}_i \equiv \frac{N_i}{D_i} U_i + \bar{d}_i = \frac{b}{s^2 + as} U_i + \bar{d}_i, \quad (4.3)$$

where N_i and D_i – numerator and denominator polynomials of G_i , respectively.

Then suggested control signal is formed as follows

$$T_i = N_i U_i = D_i \Theta_i - D_i \bar{d}_i \quad (4.4)$$

For simplicity the subscript i identifying the dynamic channel can be omitted resulting in the following differential equation when (4.4) is presented in the time domain

$$T = \Theta'' + a\Theta' + d, \quad (4.5)$$

where a new disturbance term is $d = D_i \bar{d}_i$.

The proposed control system for each dynamic channel has a unity gain feedback and three modules: conventional controller, adaptive feedback and feedforward controllers in the following form

$$T = [l_0 \int e dt + l_1 e] + [k_0 e + k_1 e'] + [q_0 \Theta_r + q_1 \Theta_r' + q_2 \Theta_r''], \quad (4.6)$$

where l_i , k_i , and q_i – controller gains.

System configuration for one channel is presented in Fig. 4.3.

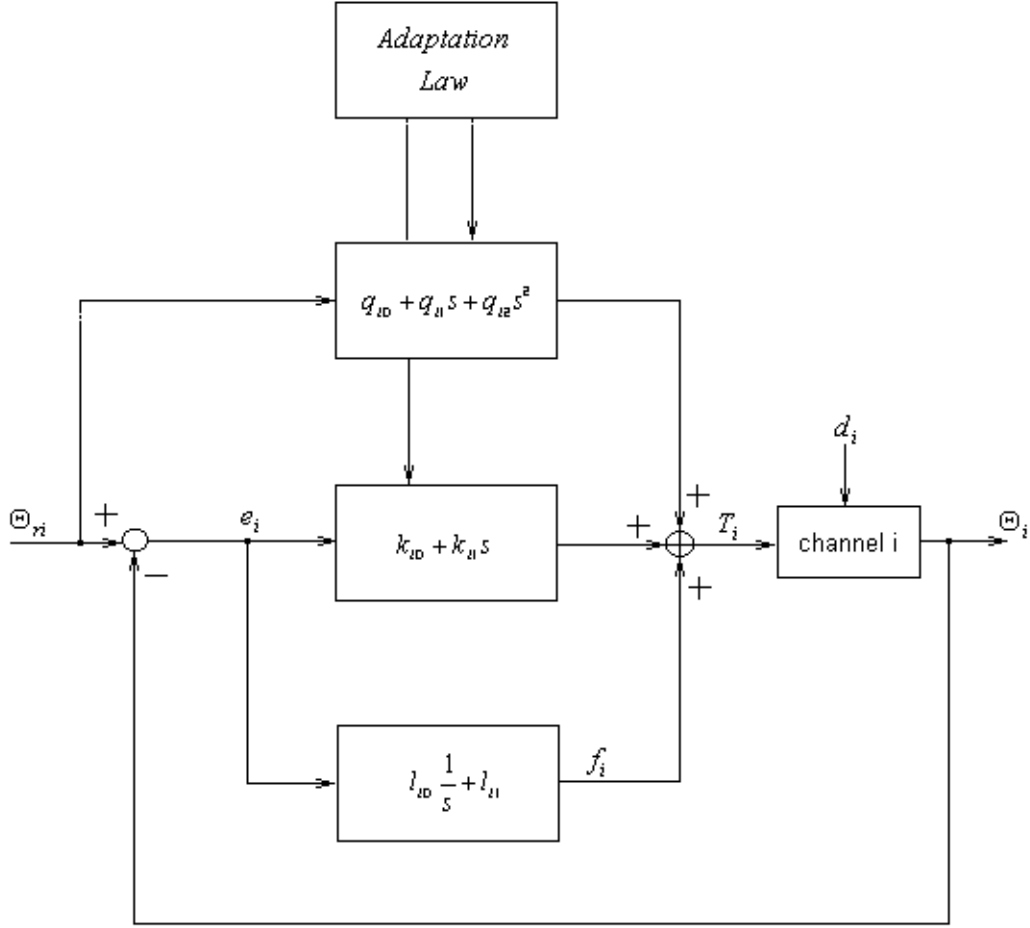


Figure 4.3. Decentralized adaptive control system

Substituting the first term of the above equation with f , as shown in Fig. 3, and combining (4.5) and (4.6) results in

$$e'' + (a + k_1)e' + k_0e = d - f - q_0\Theta_r - (q_1 - a_1)\Theta_r' - (q_2 - 1)\Theta_r'' \quad (4.7)$$

The above second-order differential equation has a matrix-vector equivalent that could be obtained by introducing $X = [e \ e']^T$, as follows

$$\dot{X} = \begin{bmatrix} 0 & 1 \\ -k_0 & -a - k_1 \end{bmatrix} X + \begin{bmatrix} 0 \\ d - f \end{bmatrix} + \begin{bmatrix} 0 \\ -q_0 \end{bmatrix} \Theta_r + \begin{bmatrix} 0 \\ a_1 - q_1 \end{bmatrix} \Theta_r' + \begin{bmatrix} 0 \\ 1 - q_2 \end{bmatrix} \Theta_r'' \quad (4.8)$$

If vector $X_m = [e_m \ e_m']^T$ represents the desired error signals, then its dynamics of convergence towards zero can be described by the following state equation written in the canonical-controllable form.

$$\dot{X}_m = DX_m = \begin{bmatrix} 0 & 1 \\ -a_0^m & -a_1^m \end{bmatrix} X_m \quad (4.9)$$

Since (4.9) is a stable system, there exists a solution to the Lyapunov equation [10]

$$PD + D^T P = -Q,$$

where P and Q – positive definite matrices.

Introduction of vector $E = X_m - X$ leads to a formal mathematical definition of the process of error convergence

$$\begin{aligned} \dot{E} = & \begin{bmatrix} 0 & 1 \\ -a_0^m & -a_1^m \end{bmatrix} E + \begin{bmatrix} 0 & 1 \\ k_0 - a_0^m & a + k_1 - a_1^m \end{bmatrix} X + \\ & + \begin{bmatrix} 0 \\ f - d \end{bmatrix} + \begin{bmatrix} 0 \\ q_0 \end{bmatrix} \Theta_r + \begin{bmatrix} 0 \\ q_1 - a \end{bmatrix} \Theta_r' + \begin{bmatrix} 0 \\ q_2 - 1 \end{bmatrix} \Theta_r'' \end{aligned} \quad (4.10)$$

A control law based on a Lyapunov function obtained from (4.10) would ensure that, given any initial condition, E converges asymptotically, and; therefore, the actual error trajectory X will track the desired error trajectory X_m that converges to zero. Consider the following positive-definite function as a Lyapunov candidate.

$$\begin{aligned} V = E^T P E + Q_0 (f - d)^2 + Q_1 (k_0 - a_0^m)^2 + Q_2 (a + k_1 - a_1^m)^2 + \\ + Q_3 q_0^2 + Q_4 (q_1 - a)^2 + Q_5 (q_2 - 1), \end{aligned} \quad (4.11)$$

where Q_i – positive scalars.

Its derivative must be negative-definite in order to claim that (4.11) is a Lyapunov function. For obtaining an analytical expression the assumption that the controlled plant is “slowly time-varying” compared to the control effort is suggested [10]; therefore, $\dot{a} = 0$, and differentiating (4.11) along the trajectory defined by (4.10) results in

$$\begin{aligned} \dot{V} = & -E^T Q E + 2Q_0 (f - d) \dot{f} - (f - d)r + 2Q_1 (k_0 - a_0^m) \dot{k}_0 - (k_0 - a_0^m)re + \\ & 2Q_2 (a + k_1 - a_1^m) \dot{k} - (a + k_1 - a_1^m)re' + 2Q_3 q_0 \dot{q}_0 - q_0 r \Theta_r + \\ & 2Q_4 (q_1 - a) \dot{q}_1 - (q_1 - a)r \Theta_r' + 2Q_5 (q_2 - 1) \dot{q}_2 - (q_2 - 1)r \Theta_r'', \end{aligned} \quad (4.12)$$

where

$$r = w_0 e + w_1 e', \quad (4.13)$$

and w_0 and w_1 are positive weighting coefficients. Grouping terms of the equation (4.12) results in

$$\begin{aligned} \dot{V} = & -E^T Q E + (f - d)(2Q_0 \dot{f} - r) + (k_0 - a_0^m)(2Q_1 \dot{k}_0 - re) + (a + k_1 - a_1^m)(2Q_2 \dot{k} - re') + \dots \\ & + q_0(2Q_3 \dot{q}_0 - r \Theta_r) + (q_1 - a)(2Q_4 \dot{q}_1 - r \Theta_r') + (q_2 - 1)(2Q_5 \dot{q}_2 - r \Theta_r'') \end{aligned} \quad (4.14)$$

While there could be multiple solutions to the control synthesis problem that result in (4.14) being negative-definite, the most natural way to select the adaptation law is as follows.

$$\begin{aligned}
2Q_0\dot{f} - r &= 0, \\
2Q_1\dot{k}_0 - re &= 0, \\
2Q_2\dot{k}_1 - re' &= 0, \\
2Q_3\dot{q}_0 - r\Theta_r &= 0, \\
2Q_4\dot{q}_1 - r\Theta_r' &= 0, \\
2Q_5\dot{q}_2 - r\Theta_r'' &= 0,
\end{aligned} \tag{4.15}$$

Hence, the time derivative of function V becomes

$$\dot{V} = -E^T QE. \tag{4.16}$$

Solving (4.15) for unknown variables provides expressions for the conventional controller

$$f = \delta \int r dt = \delta w_0 \int e dt + \delta w_1 e = l_0 \int e dt + l_1 e \tag{4.17}$$

and equations for the adjustable gains of adaptive controllers

$$\begin{aligned}
k_0 &= \alpha_1 \int redt + k_0(0), \\
k_1 &= \alpha_2 \int re^{(1)} dt + k_1(0), \\
q_0 &= \gamma_1 \int r\Theta_r dt + q_0(0), \\
q_1 &= \gamma_2 \int r\Theta_r' dt + q_1(0), \\
q_2 &= \gamma_3 \int r\Theta_r'' dt + q_2(0),
\end{aligned} \tag{4.18}$$

where $\delta, \alpha_i, \gamma_i$ – positive adaptation gains selected by the system designer.

Results of the above mathematical analysis make it evident that this approach does not require knowledge of Omni-Wrist III dynamics. In addition, there is no explicit definition of a reference model to specify the desired behavior of the system. However, signal Θ_r applied to the input represents the desired dynamics of the system response; hence, this signal could be generated by a reference model G_M selected to satisfy the design specifications.

4.2.2. System Implementation. Application of the method of Lyapunov functions results in a highly robust controller design. However, before proceeding with a prototype implementation a couple of important issues, pertaining to system stability and performance, should be discussed. Note that the control law defined by (4.6) generates signal T_i while the physical input to the dynamic channel is U_i . A correspondence between the two signals is established by (4.4), hence

$$U_i = N_i^{-1}(s)T_i \quad (4.19)$$

It appears that by applying T_i rather than U_i the residual signal $(N_i^{-1}(s)-I)T_i$ is ignored [11]. Even if this signal is regarded as a part of component d_i , it cannot be considered “slowly time-varying,” since it includes signal T_i that has high frequency content. On the other hand, N_i is a constant coefficient, and it could be demonstrated that even if equation (4.5) is scaled by a factor of N_i and the proposed controller is described by (4.6), we could still obtain the same expressions for the conventional controller (4.17) and adjustable gains (4.18).

Another problem could be encountered because the cross-coupling effects from the actuator inputs to the azimuth/declination outputs, included in component d , are very strong. Indeed, changing only one output coordinate requires the motion of both linear actuators, and therefore, the application of voltage signals to both motors. The adaptive algorithm presented in this paper is adequately suited only for loosely coupled systems [12], [13]; therefore, additional steps must be taken to reduce the coupling effects. A decoupling filter must be introduced in the input of the system. This filter is based on the solution of the inverse pose kinematics problem [10] and transforms desired azimuth/declination angles into corresponding linear actuator coordinates. Configuration of the entire decentralized system is presented in Fig. 4.4.

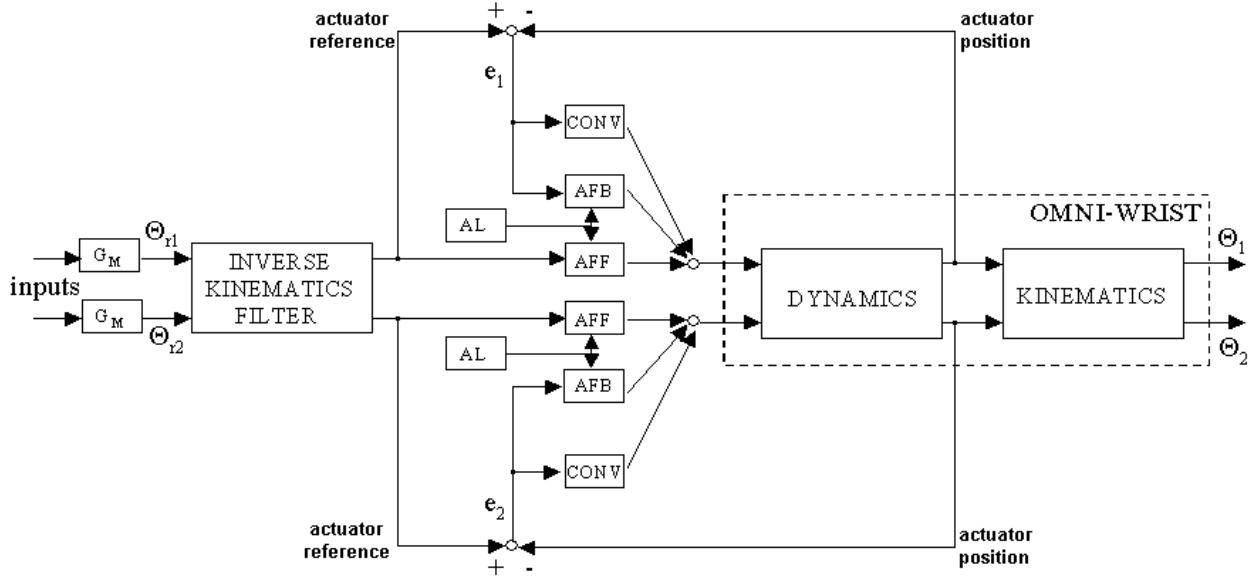


Figure 4.4. Decentralized control system
 CONV – conventional controller, AFB – adaptive feedback,
 AFF – adaptive feedforward, AL – adaptation law.

The linear actuators, represented in the above figure as DYNAMICS, take voltage as inputs and provide actuator position as outputs, generated by optical incremental encoders, which

is the reason why the controller are built around the actuators. The KINEMATICS block represents the kinematical structure of the device coupling the outputs, while the INVERSE KINEMATICS FILTER transforms the reference azimuth and declination coordinates into reference actuator positions. Each channel is controlled individually, thus facilitating decentralized operation.

4.3. BRAGG CELL CONTROL SYSTEM.

A typical configuration of an acousto-optic tracking system, such as the one shown in Fig. 3.2, includes two Bragg cells required to perform 2-dimensional beam steering and a quadrant detector, which provides beam position feedback to the controller that regulates frequencies of the RF signals.

The dynamics of a Bragg cell is characterized by a first-order transfer function given by (3.5), which is also supported by the results of our step response experiments [6], [7]. Considering that the access time of these devices could easily be on the order of tens of microseconds or less, their steering bandwidth is typically very large (usually on the order of tens of kHz). Therefore, a simple gain controller in the feedback appears to be sufficient to reject most of the distortions, and an equation for the control effort applied to a Bragg cell could be written as follows

$$f = f_c + H * v_{az,el}, \quad (4.20)$$

where $v_{az,el}$ – azimuth or elevation feedback signal from the quadrant detector.

This approach, however, does not work in practice. Any quadrant photodiode will act as a source of several types of noise, including signal shot noise, background noise, and dark current noise; while thermal noise will be generated in the electronic circuitry. System performance will be affected by all noise frequencies within the passband of the tracking system, which will pose a significant problem. Indeed, a device as agile as a Bragg cell would respond to almost any signal coming from a quadrant detector, regardless of whether the signal represents an actual displacement of the laser beam or just the additive noise. Therefore, a constant gain controller in the feedback needs to be complemented by intelligent filtering of the position measurement signal. A block diagram of the proposed control system, per channel, either azimuth or elevation, is presented in Fig. 4.5. In this example it is assumed that center frequency of the Bragg cells is 24MHz.

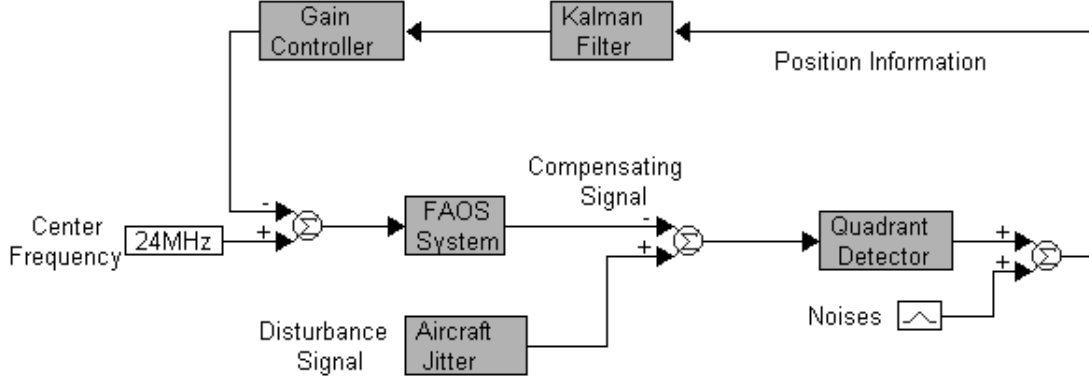


Figure 4.5. Control system configuration

A disturbance signal with a specific spectrum, e.g. representing aircraft jitter, continuously affects the pointing direction of our transmitter. If this disturbance is not completely compensated by a fast acousto-optic steering (FAOS) device, the resultant pointing angle error causes response in the quadrant detector. Since a signal from the detector is contaminated with noise, it is first filtered, and then used by a constant-gain controller to adjust the frequency of the FAOS around $f_c=24\text{MHz}$. The purpose of a Kalman filter is to estimate the state of a system from measurements, which contain random errors due to the noises in the tracking system.

Since the controlled plant (acousto-optic device) in this case is a first-order system, the implementation of a first-order Kalman filter would probably be sufficient for rejecting measurement noise. Generally, a first-order system could be expressed in the discrete-time domain as follows:

$$y_n = x_n + a \cdot y_{n-1}, \quad (4.21)$$

where x is the filter input, y – filter output, and a – parameter of the model.

Then an equation for a first-order Kalman filter is

$$y_n = \frac{M_{n|n-1}}{s + M_{n|n-1}} \cdot (x_n - a \cdot y_{n-1}) + a \cdot y_{n-1}, \quad (4.22)$$

where s is the noise variance and the adaptation mechanism of the filter is given by

$$\begin{aligned} M_{n|n-1} &= M_{n-1} \cdot a^2 + (x_n - a \cdot y_{n-1}) \\ M_n &= M_{n|n-1} \cdot \frac{1 - M_{n|n-1}}{s + M_{n|n-1}} \end{aligned} \quad (4.23)$$

The above control and adaptive filtering algorithms are iterative and could be programmed in software. The frequency at which the control inputs to the FAOS system are updated could be very high (tens of kHz or more) and is simply a function of the hardware characteristics and the latency in software-hardware interaction.

4.4. FUSION OF THE TECHNOLOGIES.

The development of a hybrid beam steering system, combining the advantages of different technologies *fused* together by advanced controls, is the approach that has a great potential. It is well understood that we need to avoid the situation when both systems work “one against another” causing unnecessary motion, power losses and resulting in positioning errors. The proposed architecture is presented in Fig. 4.6 below. An optical transceiver with a fast steerer, such as a pair of Bragg cells could be installed on a sensor mount of the Omni-Wrist gimbal.

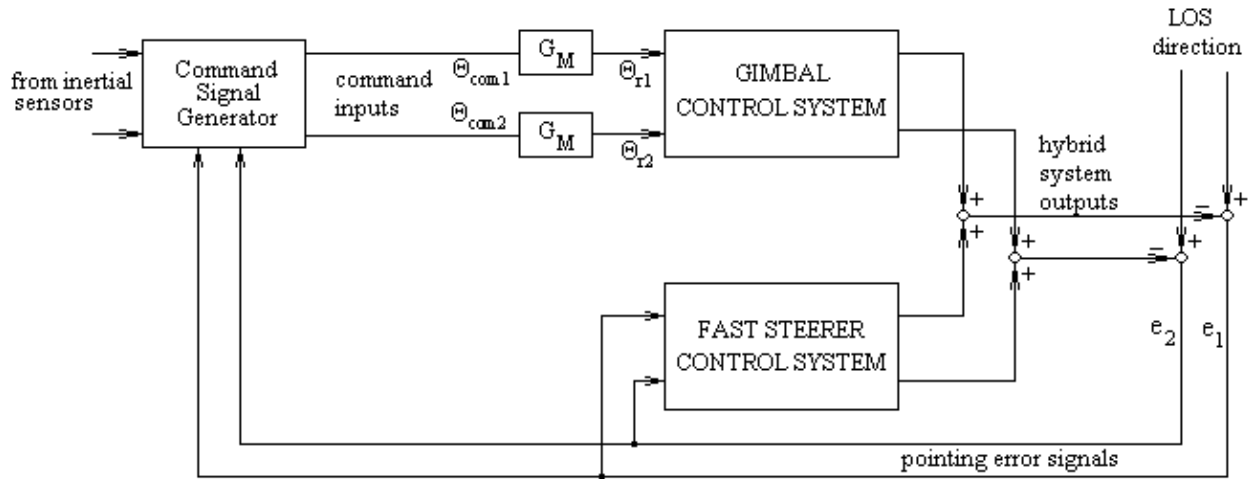


Figure 4.6. Hybrid system configuration

Coordinated operation of the proposed system could be assured by hierarchical control. As could be seen in the above figure, command inputs are only applied to the gimbal, while the line-of-sight (LOS) error, detected by a position sensing detector, is only used to control the fast steerer. This approach facilitates distribution of tasks between the two devices in a very efficient way, avoiding the situation when both are driven with the same inputs and could potentially work “one against the other.” It is also an efficient approach in the sense that command signals are typically generated to compensate for certain mechanical motion (e.g. the changing attitudes of both communicating platforms), and are usually “slow-speed-large-magnitude” signals.

Contrary, the LOS disturbance, that a position-sensing detector is able to pick, is a low-magnitude signal, which could potentially have very high frequency content (if the pointing distortion occurs due to high-frequency jitter or the effect of the optical turbulence combined with fast motion of both the transmitter and the receiver). These intrinsic properties lead to an intuitive conclusion that most of the attitude-related changes should be handled by a gimbal, while the fine LOS tracking should be primarily assigned to a fast steerer. Additional interaction between the two components of a hybrid system is still needed, and it will be discussed later in this section. Detailed operation of the system is as follows.

Command inputs in the desired coordinate system (yaw/pitch, azimuth/declination, etc.) are fed into the Reference Models with desired dynamics given by the transfer functions G_M , producing the reference vector in the desired coordinate system. The reference model vector θ_r is transformed through the Inverse Kinematics block (see Fig. 4.4) into the reference vector in the coordinates of the actuators (typically counts of the optical quadrature encoders). The controller for each axis converts the state error (difference between the state of the Reference Model in the actuator coordinates and the state of the plant) into a control signal, facilitating an exponential decay of the state error signal with predefined rate, and consequently, decoupled operation in the reference coordinates [14]. Although the resultant control law seems to be formidable, a dedicated modern PC implements it quite effortlessly, performing the computational cycle on the 20 kHz clock. The main task of the coarse steerer could be identified as platform stabilization achieved by compensating for the disturbances in the orientation of the optical platform as soon as they are detected. Detection of such disturbances could be performed, for example, by an inertial measurement unit, consisting of a 3-axis accelerometer, a 3-axis magnetometer, and a 3-axis gyroscope, also known as the MARG (Magnetic/Angular Rate/Gyro) sensor operating in tilt-compensated (strap-down) mode. The accurate estimation of the disturbance signal, used for the compensation, could be achieved by the application of a Kalman filter fusing the data collected from an inertial measurement unit. However, such work is beyond the scope of this project.

While the position control system, outlined above, is necessary to compensate for the disturbance in the orientation of the platform, optical tracking is required to maintain a robust link throughout a communication session. The main purpose of this system is to minimize the receive power losses caused by the uncertainty in the line-of-sight (LOS) direction due to

reference frame errors, errors in the pointing mechanism (boresight errors), dynamic changes of the LOS due to transmitter/receiver motion, and beam wander caused by the optical turbulence. Residual signals e_1 and e_2 , representing pointing disturbance to the LOS, must be eliminated by the fast steerer. Position measurements, performed by a quadrant detector, are always contaminated with photodetection and thermal noises; therefore, these signals are passed through a Kalman filter prior to being applied to the Bragg cells, as shown in Fig. 4.5. The errors are used to adjust the ultrasonic frequencies of the devices around $f_c=24\text{MHz}$ to perform agile beam steering.

It should be well understood that the driving mechanisms for the robotic manipulator must be controlled not only by the platform stabilization system, but also by the optical tracking system. Command Signal Generator, shown in Fig. 4.6, is responsible for computation of the gimbal's command inputs based on both the inertial measurements and the pointing errors measured by the quadrant detector. The first component is necessary to assure that the gimbal compensates for the changes in the orientation of its own optical platform, while the second component is required to track the motion of the other communication terminal, which could very well be outside the range covered by the fast steerer. Therefore, the function of the Command Signal Generator could be expressed in the form

$$\begin{bmatrix} \Theta_{com1} \\ \Theta_{com2} \end{bmatrix} = - \left(\begin{bmatrix} \Theta_{i1} \\ \Theta_{i2} \end{bmatrix} + f^* \left\{ \begin{bmatrix} e_1 \\ e_2 \end{bmatrix} - e_{TR} \right\} \right), \quad (4.24)$$

where Θ_{i1} and Θ_{i2} are angular estimates from the inertial sensors, e_1 and e_2 are the pointing errors, e_{TR} is the threshold determined by a practical range of the fast steerer, and function f^* is defined as follows

$$f^*\{x\} = \begin{cases} x, & \text{if } x > 0 \\ 0, & \text{otherwise} \end{cases} \quad (4.25)$$

The threshold errors in (4.24) should be chosen carefully to avoid a situation when the Bragg cells could reach their saturation limits and not be able to compensate for the low-magnitude-high-frequency angular perturbations to the LOS in both azimuth and elevation channels.

4.5. SIMULATION RESULTS.

The designed hybrid steering system has been tested under various operating conditions, which could arise from motion of the communicating platforms, as well as the adverse effects of

the mechanical vibrations (jitter) or the effects of the optical turbulence, resulting in the change of the beam direction. The results of this simulation study, conducted using MATLAB/SIMULINK models of the system components, are summarized below.

First, the gimbal control system was designed and tested. The selected goal was to achieve the settling time $T_{set} = 50\text{ms}$ with no overshoot, which places the poles of the closed-loop system at $-80 \pm j$, resulting in the following transfer function of the reference model (see Fig. 4.4)

$$G_m(s) = \frac{6401}{s^2 + 180s + 6401} \quad (4.26)$$

Fig. 4.7 features response of the gimbal to a square-wave-shaped command applied to the azimuth input. The adaptation effects are clearly seen during each excursion of the output signals, which track the desired trajectory closer as time goes on.

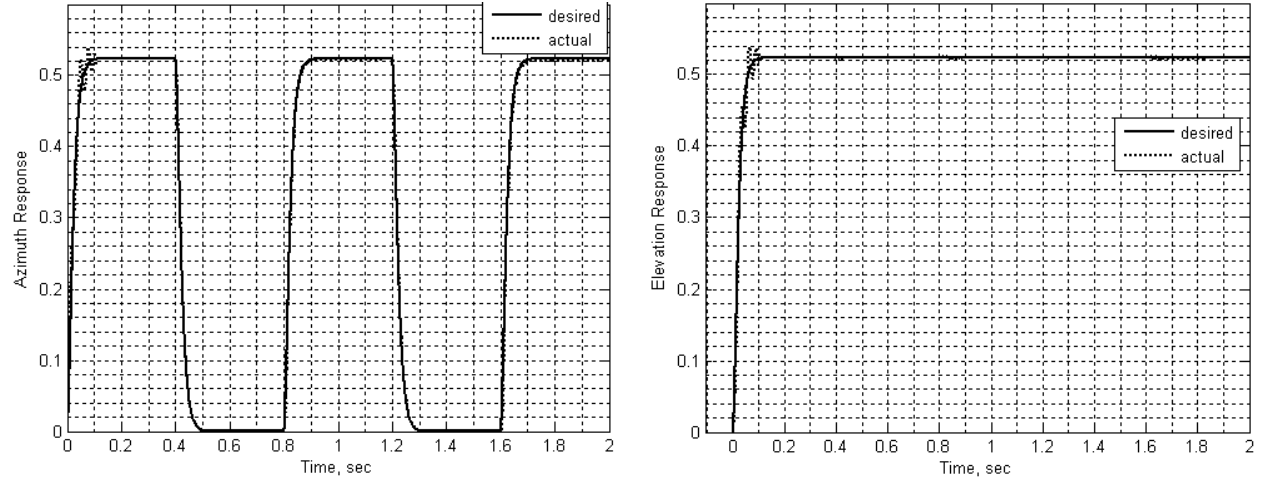


Figure 4.7. Response of the gimbal control system to a square wave signal applied to the azimuth channel

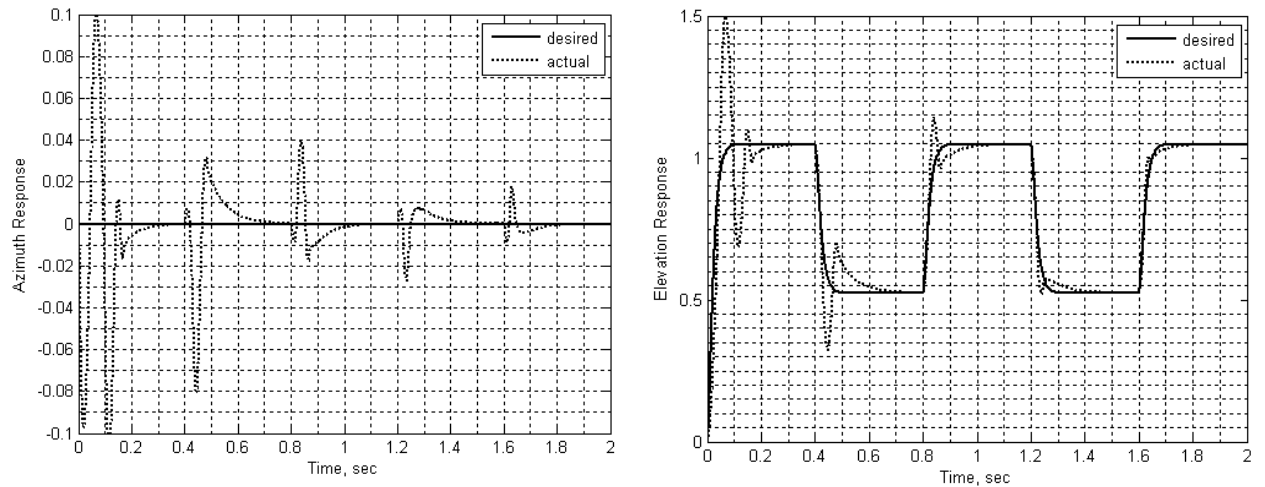


Figure 4.8. Response of the gimbal control system to a square wave signal applied to the elevation channel

Similar results could be observed when the elevation command is changed as shown in Fig. 4.8.

Next, a hybrid steering system was assembled in the simulation environment according to the architecture in Fig. 4.6. In addition to the control commands, used in the previous two simulations, the outputs were contaminated with zero-mean additive noise, emulating the effects of the pointing errors caused by the platform jitter and the optical turbulence. To represent a realistic environment, perturbations to the LOS in both azimuth and elevation channels were chosen to have Gaussian PDFs, thus resulting in the radial pointing errors having Rayleigh distribution. An important aspect of a tracking experiment is the choice of the spectral characteristics of a disturbance signal. It could be, for example, recorded vibration spectra from satellites, aircraft, ground vehicles, etc. All these characteristics have very particular shapes, possibly with resonant peaks, representing operation of specific subsystems onboard the communication platform as well as its motion patterns.

For the purpose of our study, we chose a more generalized spectrum. A disturbance signal was formed by filtering random noise with a second-order low-pass filter with a bandwidth of 2kHz. This results in almost flat spectrum extending to 2kHz, which exceeds the effects of most of the realistic environments, where precise pointing of a laser beam is adversely affected by vibrations and atmospheric effects. A sample of the temporal data, representing the jitter affecting the optical platform, is shown in Fig. 4.9. Also shown in the figure below is response of the hybrid steering system compensating the effects of the jitter.

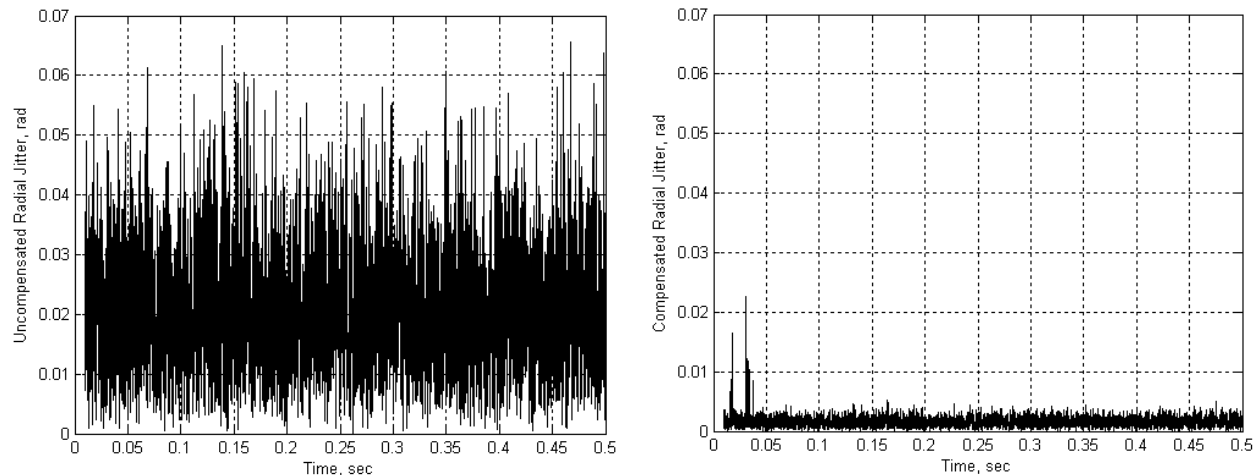


Figure 4.9. Temporal response of the system to high-frequency jitter without compensation and with hybrid tracking

Fig. 4.10 features the spectral content of the jitter, shown in a solid line, as well as the frequency characteristics of the designed system compensating for the effects of the jitter (dash-dotted line).

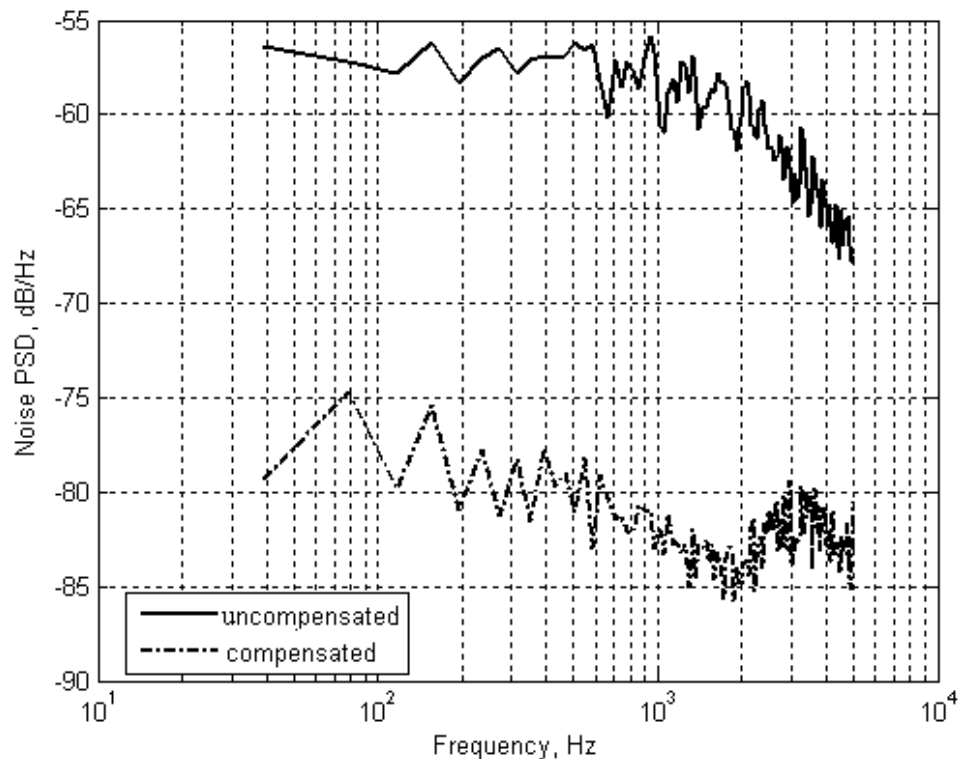


Figure 4.10. Spectral response of the hybrid steering system

Finally, system performance was tested when control commands are applied to the inputs, while the outputs are subjected to the jitter noise. These results are presented in Fig. 4.11 and Fig. 4.12 for azimuth command and elevation command, respectively.

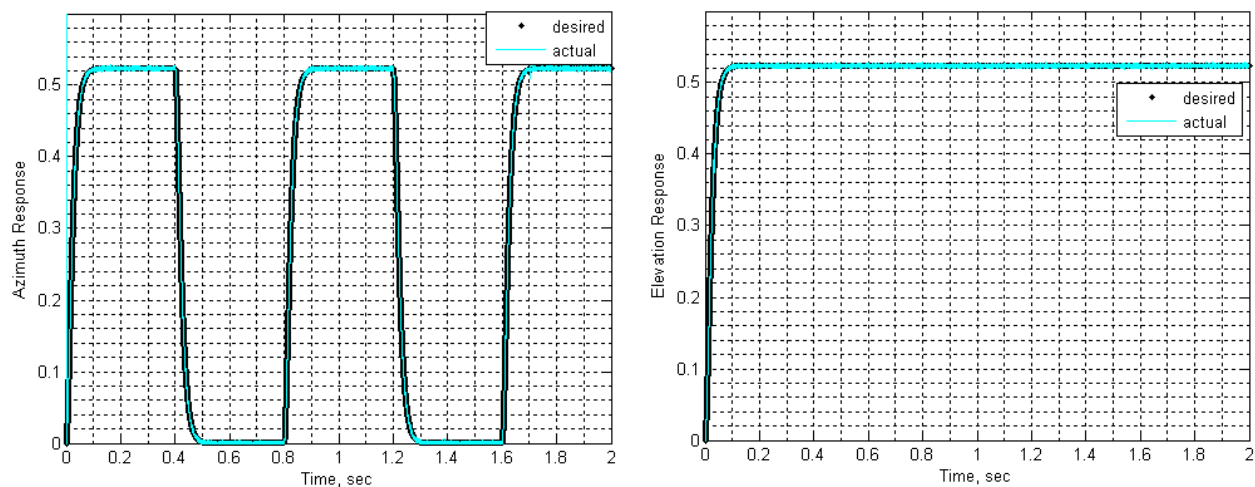


Figure 4.11. Response of the hybrid control system to a square wave signal applied to the azimuth channel

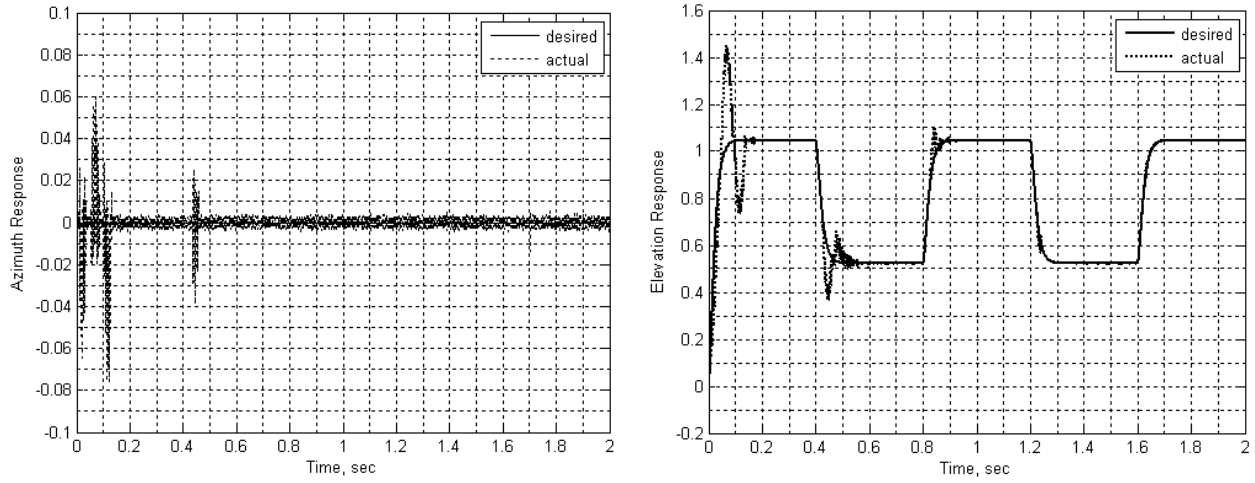


Figure 4.12. Response of the hybrid control system to a square wave signal applied to the elevation channel

It is evident from the above figures that the adaptation process is accelerated and the tracking capabilities of the hybrid system are noticeably enhanced.

Additional analysis of the temporal and spectral data presented in Fig. 4.9 and Fig. 4.10 reveals that the variance of the uncompensated jitter is $0.1232 \times 10^{-3} \text{ rad}^2$. When the hybrid system is enabled, the variance reduces to $0.1132 \times 10^{-5} \text{ rad}^2$, or approximately by a factor of 108.8. The associated reduction of the pointing error in the link budget equation may be used in several ways, including the increase of the link margin, extending the link range, reduction of the transmit power, etc.

5. ADDITIONAL CONSIDERATIONS FOR QUANTUM COMMUNICATION SYSTEMS

Quantum communication, a preferred modality when security of a data link is extremely important, presents additional challenges in the development of a pointing, acquisition and tracking (PAT) system. These challenges, not typically encountered in conventional laser communications, may include, but not be limited to, wavelength issues, using separate sources for tracking and communication, polarization of the transmitted signal, etc.

5.1. WAVELENGTH COMPATIBILITY.

When very low transmit signal levels are used to send data, tracking on the communication beam becomes impossible and the second laser source is needed to send a beacon signal. The extreme situation occurs when single photons are used to encode the bits of information. The second laser source must have a different wavelength from that of the communication signal, so that they could be spectrally separated by the receiver. While sending two aligned beams at different wavelengths is generally not a problem, in our proposed approach it becomes a significant challenge. The Bragg cells deflect each beam at an angle, which is a function of the wavelength, as could be seen from (3.5).

The situation could be alleviated if the two sources are chosen in such a way that their wavelength ratio is 2:1. As a practical example, it should be possible to use a 775nm laser source, and a beam splitter to divide the source power between two optical trains. Then in one of the trains we can down-convert 775nm into 1550nm wavelength, which can be used as a beacon signal without having to worry about its high power levels, since this wavelength is considered to be “eye-safe.” The other wavelength, 775nm, which could be used to encode binary information, is not eye-safe; however, the transmit power used in quantum communications is always within the harmless range.

Both wavelengths could be aligned and steered in exactly the same direction by the Bragg cells if we use the first diffracted order of 1550nm to perform tracking, and the second diffracted order of the 775nm wavelength for communication, for which all angles in (3.5) will be doubled. The only concern about using the higher diffracted order for the communication carrier is the efficiency and the available power in the transmitted signal. To describe energy distribution over the scattered orders of the Bragg cell, a set of coupled differential equations [15], [16] can be considered

$$\frac{dE_n}{d\xi} = \frac{-j\alpha}{2} \{e^{-j(n-1)Q\xi} E_{n-1} + e^{jnQ\xi} E_{n+1}\} \quad (5.1)$$

where n is the order of the scattered beam, α - phase peak delay in the medium, and ξ is the normalized position of the beam inside the cell.

To emphasize on the beam intensities on the output of the AOD we set $\xi = 1$. The phase peak delay is defined as

$$\alpha = \frac{Ck_m SL}{2}, \quad (5.2)$$

where k_m is the light wave number, S - acoustic field amplitude, L is interaction length of the cell defined by the transducer size, and constant parameter C is defined in [17].

When $Q \gg 2\pi$, the cell is considered to be in the Bragg regime. In reality, Q is finite and in many instances can be slightly greater than 2π (this especially applies to the case when a large steering range needs to be achieved). The general trend is to concentrate the optical energy in the immediate spatial neighborhood of the zeroth order. Therefore, truncation of much weaker higher diffracted orders creates negligible numerical errors. Applying (5.1) to the first five scattered orders, we obtain the following equations for $E_{-2}, E_{-1}, E_0, E_1, E_2$ [15]:

$$\begin{aligned} \frac{dE_2}{d\xi} &= \frac{-j\alpha}{2} \{e^{-jQ\xi} E_1 + e^{j2Q\xi} E_3\} \\ \frac{dE_1}{d\xi} &= \frac{-j\alpha}{2} \{E_0 + e^{jQ\xi} E_2\} \\ \frac{dE_0}{d\xi} &= \frac{-j\alpha}{2} \{e^{jQ\xi} E_{-1} + E_1\} \\ \frac{dE_{-1}}{d\xi} &= \frac{-j\alpha}{2} \{e^{j2Q\xi} E_{-2} + e^{-jQ\xi} E_0\} \\ \frac{dE_{-2}}{d\xi} &= \frac{-j\alpha}{2} \{e^{j3Q\xi} E_{-3} + e^{-j2Q\xi} E_{-1}\} \end{aligned} \quad (5.3)$$

The set of coupled differential equations given by (5.1) can be solved numerically for a given number of diffracted orders to demonstrate how the change of Q affects intensity distribution among them. The following two figures show how intensities vary when a Klein-

Cook parameter is changed, and the phase peak delay is assumed to be equal to 4. For the sake of simplicity only six diffracted orders are used along with the non-diffracted order.

Fig. 5.1 presents numerical results for $Q=2\pi$. It is seen from the figure that there is a noticeable amount of intensity in scattered orders. At the output of the Bragg cell intensity of the first diffracted order is approximately 84% of that of the incident light (which corresponds to 84% diffraction efficiency). The remaining 16% is distributed among the other diffracted beams. The situation presented in Fig. 5.1 illustrates that by selecting a proper value for \hat{a} we can put a significant portion of the beam intensity into the first order.

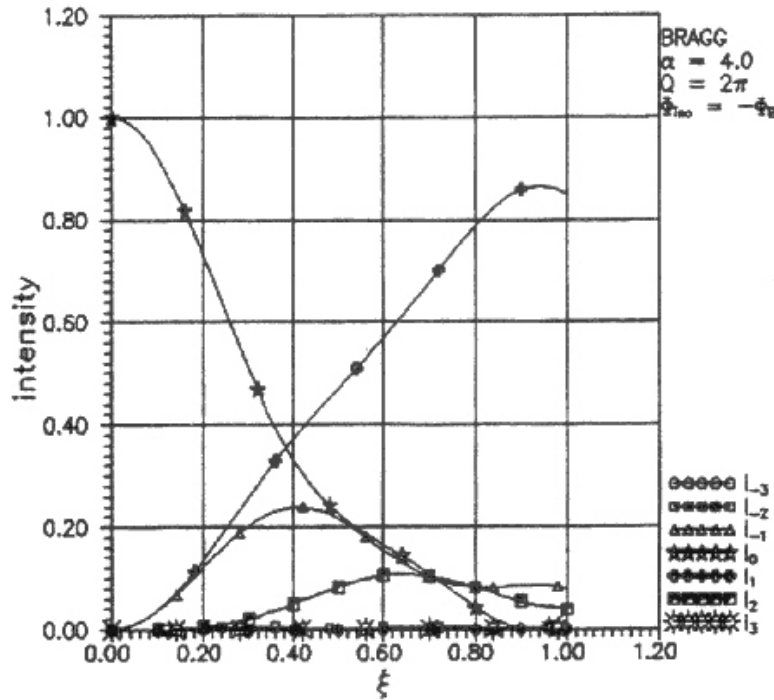


Figure 5.1. Intensity distribution for $Q=2\pi$

Fig. 5.2 presents numerical solution results when the Klein-Cook parameter is changed to 4π and the system is “deeper” in the Bragg regime. As can be seen from this numerical solution, higher-order diffracted beams start “fading” compared to those in Fig. 5.1. At the same time intensity of the first order diffracted beam at the output of the Bragg cell practically does not change and stays around 84% of the incident light intensity.

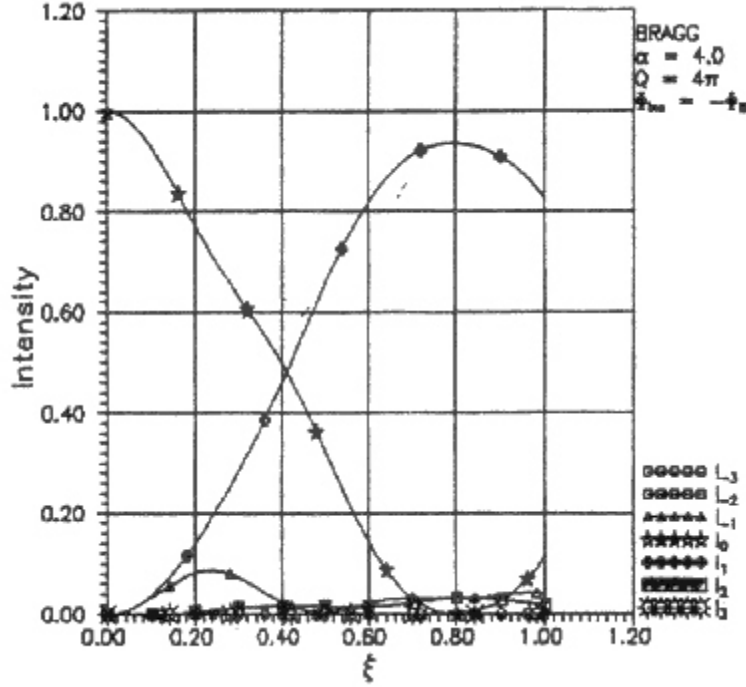


Figure 5.2. Intensity distribution for $Q = 4\pi$

Analysis of the above figures as well as the results presented in [18], [19] leads to a conclusion that it is possible to design an acousto-optic beam steerer that will offer high efficiency for the first diffracted order at one wavelength (1550nm) and acceptable efficiency for the second diffracted order at the other wavelength (775nm). For single-photon transmission the output power for the communication signal only needs to be

$$P_t = h\nu * B, \quad (5.4)$$

where $h\nu$ is the energy of a photon and B is the bit rate.

For 1Gbit/s transmission the above value needs to be as little as $2.56 \times 10^{-10} \text{ W}$ or -65.9 dBm .

5.2. POLARIZATION COMPATIBILITY.

When two orthogonal polarizations are used as the base quantum states for exchanging secret information, maintaining their orientation on the transmitter side is a critical task. One challenge is presented by the acousto-optic Bragg cells, which require specific polarization of the incident beam and rotate its plane by 90 deg. upon diffraction, as illustrated in Fig. 5.3(a). This makes polarization-based data encoding difficult, since this process must precede the beam steering. Furthermore, analysis of the robotic manipulator, used in our system, reveals that in the process of operation its optical mount continuously changes the roll orientation, as could be seen in Fig. 5.3(b). Finally, the changing attitude of the communication platform, as a result of vehicle

or aircraft motion and maneuvering, could also rotate the plane of polarization of the transmitted signal, which inevitably leads to a change in the polarization base.

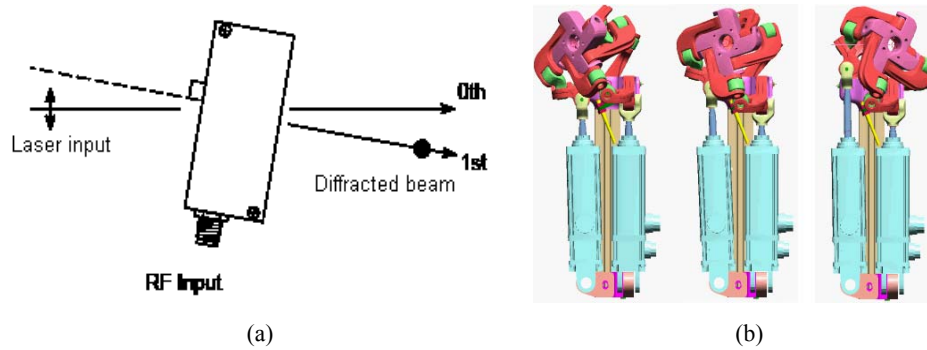


Figure 5.3. Challenges for maintaining orientation of the polarization state in transmitted signals
 (a) Specific polarization of input and output signals of acousto-optic deflectors
 (b) Varying roll angle of gimbal's pointing mechanism (cross-shaped optical mount)

The first problem, associated with the use of the acousto-optic devices, could be solved by implementing a polarization diversity steerer featured in Fig. 5.4. This is a relatively simple modification of the optical setup, which requires twice as many acousto-optic devices, but works

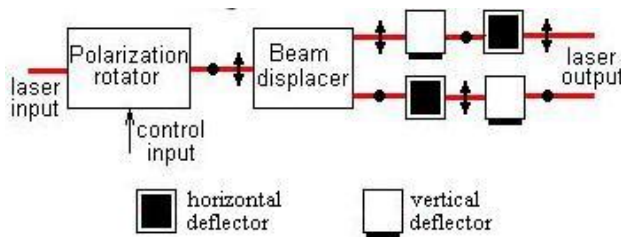


Figure 5.4. Acousto-optic system utilizing diversity approach to steer a beam with arbitrary polarization

for an arbitrary polarization of the incident signal. To address the second challenge outlined in this section and maintain integrity of the base quantum states it may be necessary to develop a technology for polarization tracking. To

implement such system, mathematical modeling techniques and sensory data of the PAT system must be used for calculating the control input signal of the polarization rotator.

The proposed hybrid steering device relies on the information from the MARG sensor, mentioned in Section 4.4, which provides complete information on the orientation of the communication platform. This information could also be used to compute rotation of the linear polarization planes associated with the changing attitude of the ground-based or the airborne vehicle. Furthermore, additional rotation induced in the beam steering process performed by the gimbal could be found by analyzing the kinematics of the device and developing a mathematical model relating gimbal control inputs to the resulting pitch, yaw, and roll coordinates of the optical mount. The concept of the proposed system is illustrated in Fig. 5.5. Precise orientation of the polarization planes of the transmitted signal could be maintained in real time, considering

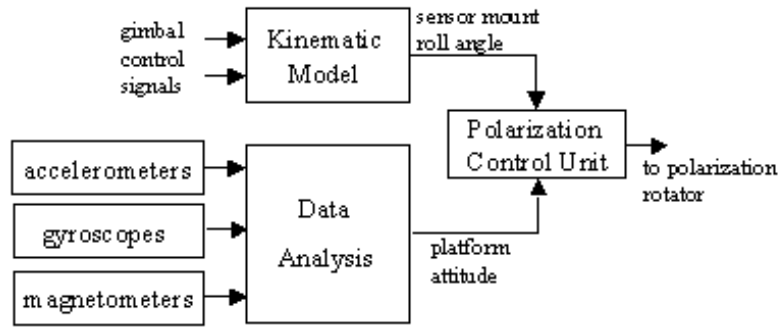


Figure 5.5. System for real-time compensation of polarization base distortions that currently available electro-optical rotators offer adequate dynamic performance with respect to the time scale of mechanical motion.

While most of the approaches to make the proposed hybrid technology compatible with quantum communication, as discussed in this chapter, constitute possible future research; the development of a polarization tracking system is within the framework of this extension project.

6. POLARIZATION CONTROL

Polarization control system has two major components: one associated with the estimation of the communication platform attitude, which could change as a result of motion, and another one addressing rotation of the moving platform, which performs pointing of the optical telescope.

6.1. PLATFORM ATTITUDE ESTIMATION.

6.1.1. Inertial Sensors. The PAT system is required to compensate for the vibrations applied to the optical platform while the air or ground vehicle is in motion. The degradation of the performance of the communications system is mitigated through the proper application of advanced control laws. For example, additional feed-forward vibration rejection control system [20] could be used that utilizes a set of inertial navigation sensors to measure the optical platform orientation disturbance and calculates the control effort that drives the actuators of the Omni-Wrist III. The signals from the inertial navigational unit, consisting of a 3-axis gyroscope, 3-axis accelerometer, and a 3-axis magnetic sensor, are ‘fused’ to form a quaternion representation of the orientation of the optical platform. The control system compensates for the disturbance in the orientation of the optical platform as soon as it is detected due to the feedforward mode of operation (in a feedback configuration, such as the optical tracking, the disturbance is rejected after it degrades the performance of the communications system). The development of an Extended Kalman filter ‘fusing’ the inertial navigation sensor data is presented below.

The performance of any vibration rejection system, and consequently the communications system, relates directly to the disturbance measurement. Within the scope of another project, an inertial measurement unit was designed utilizing a 3-axis accelerometer, a 3-axis magnetometer, and a 3-axis gyroscope. The MARG (Magnetic/Angular Rate/Gyro) sensor operates in tilt-compensated (strap-down) mode.

The magnetic measurements are collected from a Honeywell HMC1023 3-axis magneto-resistive sensor. The acceleration measurements are facilitated by a two-axis Analog Devices ADXL203 MEMS sensor and a perpendicularly mounted Analog Devices ADXL103 single-axis MEMS sensor. The angular rate information is provided by three perpendicularly mounted Analog Devices ADXRS150 MEMS sensors. The use of three types of sensors is justified by the unacceptable errors limiting the usability of an inertial navigation system equipped with a single type or any combination of two types of sensors. The magnetic sensors in conjunction with the

accelerometers provide orientation information that is flawed in the presence of acceleration other than gravity and/or in the presence of a magnetic field other than that of the Earth, while orientation integrated from the angular rates measured by the gyroscopes is exposed to errors originating from the zero drift of the sensors [21]. The scenario, in which the errors originating from different sources distort the orientation vector provided by the accelerometers and magnetic sensors and the orientation vector calculated from the data collected from the gyroscopes, calls for the application of the Kalman filter and ‘fusing’ of data collected from all the sensors into a single orientation vector.

6.1.2. Quaternions. Reliable operation of the orientation measurement subsystem is dependent on proper representation of the state of the system. Quaternion representation, widely used in navigation systems and computer graphics, was selected due to its singularity-free characterization of orientation. Basic concepts related to manipulation with quaternions utilized in this project are summarized below:

Quaternions, numbers with three imaginary parts, can be described as an extension of complex numbers (with only one imaginary part). Similarly to a complex number $c = a + \mathbf{i}b$ given by two real numbers a and b , where \mathbf{i} is the imaginary unit defined as $\mathbf{i}^2 = -1$, a quaternion $\mathbf{q} = q_w + \mathbf{i}q_x + \mathbf{j}q_y + \mathbf{k}q_z$ is given by four real numbers q_w, q_x, q_y , and q_z and three imaginary units defined as $\mathbf{i}^2 = \mathbf{j}^2 = \mathbf{k}^2 = \mathbf{ijk} = -1$. Quaternions are well suited for representation of spatial rotation thanks to their compact notation, relatively simple operators, and the singularity-free property [22]. A rotation around an axis specified by vector \mathbf{v} defined as

$$\mathbf{v} = [v_x \quad v_y \quad v_z]^T \quad (6.1)$$

by angle θ is expressed in quaternion form as

$$\mathbf{q} = \cos\left(\frac{\theta}{2}\right) + \mathbf{i}\sin\left(\frac{\theta}{2}\right)v_x + \mathbf{j}\sin\left(\frac{\theta}{2}\right)v_y + \mathbf{k}\sin\left(\frac{\theta}{2}\right)v_z. \quad (6.2)$$

Two consecutive rotations corresponding to quaternions $\mathbf{q}_1 = q_{w1} + \mathbf{i}q_{x1} + \mathbf{j}q_{y1} + \mathbf{k}q_{z1}$ and $\mathbf{q}_2 = q_{w2} + \mathbf{i}q_{x2} + \mathbf{j}q_{y2} + \mathbf{k}q_{z2}$ can be represented by quaternion $\mathbf{q} = q_w + \mathbf{i}q_x + \mathbf{j}q_y + \mathbf{k}q_z$ given by quaternion product $\mathbf{q} = \mathbf{q}_1 \mathbf{q}_2$ calculated as

$$\begin{aligned}
q_w &= q_{w1}q_{w2} - q_{x1}q_{x2} - q_{y1}q_{y2} - q_{z1}q_{z2} \\
q_x &= q_{w1}q_{x2} + q_{x1}q_{w2} + q_{y1}q_{z2} - q_{z1}q_{y2} \\
q_y &= q_{w1}q_{y2} + q_{y1}q_{w2} + q_{z1}q_{x2} - q_{x1}q_{z2} \\
q_z &= q_{w1}q_{z2} + q_{z1}q_{w2} + q_{x1}q_{y2} - q_{y1}q_{x2}.
\end{aligned} \tag{6.3}$$

In this paper, numerical integration of the 3-axis angular velocity signal into quaternion-specified orientation is implemented using quaternion multiplication. If the current pose is represented by quaternion \mathbf{q}_k and the angular displacement during the last iteration is given by quaternion $\mathbf{q}_{\omega k}$ defined as

$$\mathbf{q}_{\omega k} = \cos\left(\frac{1}{2}|\omega_k|T_s\right) + \mathbf{i} \sin\left(\frac{1}{2}|\omega_k|T_s\right) \frac{\omega_{x_k}}{|\omega_k|} + \mathbf{j} \sin\left(\frac{1}{2}|\omega_k|T_s\right) \frac{\omega_{y_k}}{|\omega_k|} + \mathbf{k} \sin\left(\frac{1}{2}|\omega_k|T_s\right) \frac{\omega_{z_k}}{|\omega_k|}, \tag{6.4}$$

where T_s is the sampling time and

$$|\omega_k| = \sqrt{\omega_{x_k}^2 + \omega_{y_k}^2 + \omega_{z_k}^2} \tag{6.5}$$

is the magnitude of the angular rate calculated from the constituting axes measurements, then the new pose can be calculated as

$$\mathbf{q}_{k+1} = \mathbf{q}_{\omega k} \mathbf{q}_k. \tag{6.6}$$

Equation (6.6) facilitating the quaternion multiplication given by (6.3) can be expressed in matrix-vector form as

$$\begin{bmatrix} q_w \\ q_x \\ q_y \\ q_z \end{bmatrix}_{k+1} = \begin{bmatrix} q_w & -q_x & -q_y & -q_z \\ q_x & q_w & q_z & -q_y \\ q_y & -q_z & q_w & q_x \\ q_z & q_y & -q_x & q_w \end{bmatrix}_k \begin{bmatrix} q_w \\ q_x \\ q_y \\ q_z \end{bmatrix}_{\omega k} = \begin{bmatrix} q_w & -q_x & -q_y & -q_z \\ q_x & q_w & q_z & -q_y \\ q_y & -q_z & q_w & q_x \\ q_z & q_y & -q_x & q_w \end{bmatrix}_k \begin{bmatrix} \cos\left(\frac{1}{2}|\omega_k|T_s\right) \\ \sin\left(\frac{1}{2}|\omega_k|T_s\right) \frac{\omega_{x_k}}{|\omega_k|} \\ \sin\left(\frac{1}{2}|\omega_k|T_s\right) \frac{\omega_{y_k}}{|\omega_k|} \\ \sin\left(\frac{1}{2}|\omega_k|T_s\right) \frac{\omega_{z_k}}{|\omega_k|} \end{bmatrix} \tag{6.7}$$

and linearized for small values of angular displacement as

$$\begin{bmatrix} q_w \\ q_x \\ q_y \\ q_z \end{bmatrix}_{k+1} \cong \begin{bmatrix} q_w & -q_x & -q_y & -q_z \\ q_x & q_w & q_z & -q_y \\ q_y & -q_z & q_w & q_x \\ q_z & q_y & -q_x & q_w \end{bmatrix}_k \begin{bmatrix} 1 \\ \frac{1}{2}T_s\omega_{x_k} \\ \frac{1}{2}T_s\omega_{y_k} \\ \frac{1}{2}T_s\omega_{z_k} \end{bmatrix}. \tag{6.8}$$

Equation (6.8) can also be expressed in a form convenient for the formation of the state transition matrix as

$$\mathbf{q}_{k+1} = \mathbf{q}_k + \mathbf{G}_k \boldsymbol{\omega}_k, \quad (6.9)$$

where

$$\mathbf{G}_k = \frac{1}{2} T_s \begin{bmatrix} -q_x & -q_y & -q_z \\ q_w & q_z & -q_y \\ -q_z & q_w & q_x \\ q_y & -q_x & q_w \end{bmatrix}_k. \quad (6.10)$$

6.1.3. Kalman Filter. The Kalman filter is an optimal estimator that can be successfully utilized to combine data with different distributions into a state vector describing a process with a given variance. In the following text, a Kalman filter is derived that provides an optimal estimate of the state vector from the data collected from the MARG sensor. Due to the nonlinear relationship between the state and the observation, an Extended Kalman filter linearizing the state-observation relationship around the operating point needs to be applied. The procedure leading to the construction of the Kalman filter consists of the following steps: First, the state and observation vectors are defined. The state of the system is described by the state vector \mathbf{x} as

$$\mathbf{x} = [q_w \ q_x \ q_y \ q_z \ \omega_x \ \omega_y \ \omega_z]^\top, \quad (6.11)$$

where q_w , q_x , q_y , and q_z constitute the quaternion $\mathbf{q} = q_w + \mathbf{i}q_x + \mathbf{j}q_y + \mathbf{k}q_z$ representing the orientation of the moving (sensor) frame with respect to the stationary (Earth) frame, and ω_x , ω_y , and ω_z are the angular velocities around axes x , y , and z of the moving frame. The data collected from the nine sensors forms the observation vector

$$\mathbf{z} = [m_x \ m_y \ m_z \ a_x \ a_y \ a_z \ g_x \ g_y \ g_z]^\top, \quad (6.12)$$

where m_x , m_y , and m_z are the measurements from the three axes of the magnetic field sensor, a_x , a_y , and a_z are the measurements from the three axes of the accelerometers, and g_x , g_y , and g_z are the angular velocity measurements around axes x , y , and z obtained from the three gyroscopes. Then the state transition matrix \mathbf{F} defines the development of the state of the system in time through the difference equation

$$\mathbf{x}_k = \mathbf{F}_{k-1} \mathbf{x}_{k-1} + \mathbf{w}_k, \quad (6.13)$$

where \mathbf{w}_k is the normally distributed process noise vector with covariance matrix \mathbf{Q} and k is the iteration index. The state transition matrix is defined as

$$\mathbf{F}_k = \begin{bmatrix} \mathbf{I}_4 & \mathbf{G}_k \\ 0 & \mathbf{I}_3 \end{bmatrix}, \quad (6.14)$$

where \mathbf{I}_3 and \mathbf{I}_4 are 3×3 and 4×4 identity matrices and \mathbf{G}_k is defined in (6.10). The observation vector \mathbf{z}_k is related to the state vector \mathbf{x}_k through the observation matrix \mathbf{H}_k as

$$\mathbf{z}_k = \mathbf{H}_k \mathbf{x}_k + \mathbf{v}_k, \quad (6.15)$$

where \mathbf{v}_k is the normally distributed observation noise with covariance matrix \mathbf{R} . The observation matrix can be derived from the quaternion \mathbf{q}_k representing the orientation of the moving frame with respect to the stationary frame by exploiting the fact that this quaternion transforms the magnetic field vector in Earth coordinates \mathbf{m}^E into body coordinates \mathbf{m}_k^B (measured by the magnetometers) as

$$\mathbf{m}_{k_q}^B = \mathbf{q}_k \mathbf{m}_q^E \mathbf{q}_k^{-1}, \quad (6.16)$$

while transforming the gravity vector in Earth coordinates \mathbf{a}^E into body coordinates \mathbf{a}_k^B (measured by the accelerometers) as

$$\mathbf{a}_{k_q}^B = \mathbf{q}_k \mathbf{a}_q^E \mathbf{q}_k^{-1}, \quad (6.17)$$

where vectors \mathbf{m}_k^B , \mathbf{m}^E , \mathbf{a}_k^B , and \mathbf{a}^E are represented by quaternions as

$$\mathbf{m}_{k_q}^B = \begin{bmatrix} 0 & \mathbf{i} & \mathbf{j} & \mathbf{k} \end{bmatrix} \begin{bmatrix} 0 \\ \mathbf{m}_k^B \end{bmatrix}, \mathbf{m}_q^E = \begin{bmatrix} 0 & \mathbf{i} & \mathbf{j} & \mathbf{k} \end{bmatrix} \begin{bmatrix} 0 \\ \mathbf{m}^E \end{bmatrix}, \mathbf{a}_{k_q}^B = \begin{bmatrix} 0 & \mathbf{i} & \mathbf{j} & \mathbf{k} \end{bmatrix} \begin{bmatrix} 0 \\ \mathbf{a}_k^B \end{bmatrix}, \mathbf{a}_q^E = \begin{bmatrix} 0 & \mathbf{i} & \mathbf{j} & \mathbf{k} \end{bmatrix} \begin{bmatrix} 0 \\ \mathbf{a}^E \end{bmatrix}. \quad (6.18)$$

Expressing the quaternion transformation (6.17) in equivalent matrix-vector form as

$$\mathbf{a}_k^B = \mathbf{T}_k \mathbf{a}^E, \quad (6.19)$$

where the transformation \mathbf{T}_k is related to quaternion \mathbf{q}_k as

$$\mathbf{T}_k = \begin{bmatrix} q_w^2 + q_x^2 - q_y^2 - q_z^2 & 2q_x q_y - 2q_z q_w & 2q_x q_z + 2q_y q_w \\ 2q_x q_y + 2q_z q_w & q_w^2 - q_x^2 + q_y^2 - q_z^2 & 2q_y q_z - 2q_x q_w \\ 2q_x q_z - 2q_y q_w & 2q_y q_z + 2q_x q_w & q_w^2 - q_x^2 - q_y^2 + q_z^2 \end{bmatrix}_k, \quad (6.20)$$

and substituting for the gravity vector in Earth coordinates in (6.19) as

$$\mathbf{a}^E = [0 \ 0 \ -1]^\top \quad (6.21)$$

yields

$$\mathbf{a}_k^B = \mathbf{T}_k \begin{bmatrix} 0 \\ 0 \\ -1 \end{bmatrix} = - \begin{bmatrix} 2q_x q_z + 2q_y q_w \\ 2q_y q_z - 2q_x q_w \\ q_w^2 - q_x^2 - q_y^2 + q_z^2 \end{bmatrix}_k. \quad (6.22)$$

Equation (6.22) can be linearized around the operating point given by quaternion $\mathbf{q}_k = q_{wk} + \mathbf{i}q_{xk} + \mathbf{j}q_{yk} + \mathbf{k}q_{zk}$ as

$$\mathbf{a}_k^B = \mathbf{H}_k^a [q_w \ q_x \ q_y \ q_z]_k^\top, \text{ where} \quad (6.23)$$

$$\mathbf{H}_k^a = \begin{bmatrix} q_y & q_z & q_w & q_x \\ -q_x & -q_w & q_z & q_y \\ q_w & -q_x & -q_y & q_z \end{bmatrix}_k.$$

Similarly to (6.19), the quaternion transformation (6.16) can be expressed in matrix-vector form as

$$\mathbf{m}_k^B = \mathbf{T}_k \mathbf{m}_k^E, \quad (6.24)$$

where the magnetic field vector in Earth coordinates is given as

$$\mathbf{m}_k^E = [m_x^E \ m_y^E \ m_z^E]^\top. \quad (6.25)$$

Then

$$\mathbf{m}_k^B = \mathbf{T}_k \begin{bmatrix} m_x^E \\ m_y^E \\ m_z^E \end{bmatrix} = \begin{bmatrix} m_x^E (q_w^2 + q_x^2 - q_y^2 - q_z^2) + m_y^E (2q_x q_y - 2q_z q_w) + m_z^E (2q_x q_z + 2q_y q_w) \\ m_x^E (2q_x q_y + 2q_z q_w) + m_y^E (q_w^2 - q_x^2 + q_y^2 - q_z^2) + m_z^E (2q_y q_z - 2q_x q_w) \\ m_x^E (2q_x q_z - 2q_y q_w) + m_y^E (2q_y q_z + 2q_x q_w) + m_z^E (q_w^2 - q_x^2 - q_y^2 + q_z^2) \end{bmatrix}_k. \quad (6.26)$$

Equation (6.26) can be linearized around the operating point given by quaternion $\mathbf{q}_k = q_{wk} + \mathbf{i}q_{xk} + \mathbf{j}q_{yk} + \mathbf{k}q_{zk}$ as

$$\mathbf{m}_k^B = \mathbf{H}_k^m [q_w \ q_x \ q_y \ q_z]_k^\top \quad (6.27)$$

$$\mathbf{H}_k^m = \begin{bmatrix} m_x^E q_w - m_y^E q_z + m_z^E q_y & m_x^E q_x + m_y^E q_y + m_z^E q_z & -m_x^E q_y + m_y^E q_x + m_z^E q_w & -m_x^E q_z - m_y^E q_w + m_z^E q_x \\ m_x^E q_z + m_y^E q_w - m_z^E q_x & m_x^E q_y - m_y^E q_x - m_z^E q_w & m_x^E q_x + m_y^E q_y + m_z^E q_z & m_x^E q_w - m_y^E q_z + m_z^E q_y \\ -m_x^E q_y + m_y^E q_x + m_z^E q_w & m_x^E q_z + m_y^E q_w - m_z^E q_x & -m_x^E q_w + m_y^E q_z - m_z^E q_y & m_x^E q_x + m_y^E q_y + m_z^E q_z \end{bmatrix}_k$$

$$= m_x^E \begin{bmatrix} q_w & q_x & -q_y & -q_z \\ q_z & q_y & q_x & q_w \\ -q_y & q_z & -q_w & q_x \end{bmatrix}_k + m_y^E \begin{bmatrix} -q_z & q_y & q_x & -q_w \\ q_w & -q_x & q_y & -q_z \\ q_x & q_w & q_z & q_y \end{bmatrix}_k + m_z^E \begin{bmatrix} q_y & q_z & q_w & q_x \\ -q_x & -q_w & q_z & q_y \\ q_w & -q_x & -q_y & q_z \end{bmatrix}_k.$$

Matrices \mathbf{H}_k^a and \mathbf{H}_k^m derived above relate the transformation given by quaternion \mathbf{q}_k corresponding to the orientation of the moving frame in Earth coordinates to the acceleration and magnetic field vectors in the coordinates of the moving frame. Combining the above matrices with the identity transformation between the angular velocity signals in both the observation vector and the state vector results in the formation of the whole observation matrix as

$$\mathbf{H}_k = \begin{bmatrix} \mathbf{H}_k^m & 0 \\ \mathbf{H}_k^a & 0 \\ 0 & \mathbf{I}_3 \end{bmatrix}, \quad (6.28)$$

where \mathbf{I}_3 is a 3×3 identity matrix. Having obtained a linearized state transition matrix in (6.14) and the observation matrix in (6.28), we can implement the Kalman filter as follows. The iteration begins with the prediction stage, in which a new state vector is formed by applying the state transition matrix to the previous estimate $\mathbf{x}_{k-1|k-1}$ as

$$\mathbf{x}_k = \mathbf{F}_{k-1} \mathbf{x}_{k-1|k-1} \quad (6.29)$$

and the predicted estimate covariance $\mathbf{P}_{k|k-1}$ is evaluated as

$$\mathbf{P}_{k|k-1} = \mathbf{F}_{k-1} \mathbf{P}_{k-1|k-1} \mathbf{F}_{k-1}^\top + \mathbf{Q}_k. \quad (6.30)$$

In the update stage, the innovation residual \mathbf{y}_k is found as

$$\mathbf{y}_k = \mathbf{z}_k - \mathbf{H}_k \mathbf{x}_{k|k-1} \quad (6.31)$$

with the corresponding covariance \mathbf{S}_k given by

$$\mathbf{S}_k = \mathbf{H}_{k-1} \mathbf{P}_{k|k-1} \mathbf{H}_{k-1}^\top + \mathbf{R}_k \quad (6.32)$$

leading to the formula for Kalman gain

$$\mathbf{K}_k = \mathbf{P}_{k|k-1} \mathbf{H}_{k-1}^\top \mathbf{S}_k^{-1}. \quad (6.33)$$

The state estimate is then updated as

$$\mathbf{x}_{k|k} = \mathbf{x}_{k|k-1} + \mathbf{K}_k \mathbf{y}_k \quad (6.34)$$

followed by an update of the estimate covariance

$$\mathbf{P}_{k|k} = (\mathbf{I}_7 - \mathbf{K}_k \mathbf{H}_k) \mathbf{P}_{k|k-1}, \quad (6.35)$$

where \mathbf{I}_7 is a 7×7 identity matrix.

6.2. SENSOR MOUNT ROLL ANGLE ESTIMATION.

Finding roll orientation of the sensor mount requires partial solution of the inverse kinematics problem, discussed in Section 2 of this report. In this case the azimuth and declination coordinates, known from the control efforts generated by the gimbal control system, are to be used to find the pitch, yaw and roll coordinates of the transmitting telescope.

The transformation between the stationary frame of the gimbal and the sensor mount frame through Leg A and Leg B is found using Denavit-Hartenberg parameters [2]. These transformation given by (2.1) could be expanded as follows:

$$A = A_1 \times A_2 \times A_3 \times A_4 =$$

$$\begin{bmatrix} C_1 C_4 (C_2 C_3 - S_2 S_3 C_\alpha) + & C_1 (C_2 S_3 + S_2 C_3 C_\alpha) - & C_1 S_4 (C_2 C_3 - S_2 S_3 C_\alpha) + & \\ (S_1 S_3 C_4 + C_1 S_2 S_4) S_\alpha + & S_1 C_3 S_\alpha & (S_1 S_3 S_4 - C_1 S_2 C_4) S_\alpha - & d(S_1(1 - C_\alpha) - C_1 S_2 S_\alpha) \\ S_1 S_4 C_\alpha & & S_1 C_4 C_\alpha & \\ S_1 C_4 (C_2 C_3 - S_2 S_3 C_\alpha) - & S_1 (C_2 S_3 + S_2 C_3 C_\alpha) - & S_1 S_4 (C_2 C_3 - S_2 S_3 C_\alpha) - & \\ (C_1 S_3 C_4 - S_1 S_2 S_4) S_\alpha - & S_1 C_3 S_\alpha & (C_1 S_3 S_4 + S_1 S_2 C_4) S_\alpha - & d(C_1(C_\alpha - 1) - S_1 S_2 S_\alpha) \\ C_1 S_4 C_\alpha & & C_1 C_4 C_\alpha & \\ C_4 (S_2 C_3 + C_2 S_3 C_\alpha) - & S_2 S_3 - C_2 C_3 C_\alpha & S_4 (S_2 C_3 + C_2 S_3 C_\alpha) + & \\ C_2 S_4 S_\alpha & 0 & C_2 C_4 S_\alpha & dC_2 S_\alpha \\ 0 & & 0 & 1 \end{bmatrix} \quad (6.36)$$

and

$$B = B_0 \times B_1 \times B_2 \times B_3 \times B_4 =$$

$$\begin{bmatrix} C_5 C_8 (C_6 C_7 - S_6 S_7 C_\alpha) + & -C_5 S_8 (C_6 C_7 - S_6 S_7 C_\alpha) - & C_5 (C_6 S_7 + S_6 C_7 C_\alpha) - & \\ (S_5 S_7 C_8 + C_5 S_6 S_8) S_\alpha + & (S_5 S_7 S_8 + C_5 S_6 C_8) S_\alpha + & S_5 C_7 S_\alpha & d(S_5(1 - C_\alpha) - C_5 S_6 S_\alpha) \\ S_5 S_8 C_\alpha & S_5 C_8 C_\alpha & & \\ -C_8 (S_6 C_7 + C_6 S_7 C_\alpha) + & S_8 (S_6 C_7 + C_6 S_7 C_\alpha) + & -S_6 S_7 + C_6 C_7 C_\alpha & -dC_6 S_\alpha \\ C_6 S_8 S_\alpha & C_6 C_8 S_\alpha & & \\ S_5 C_8 (C_6 C_7 - S_6 S_7 C_\alpha) - & -S_5 S_8 (C_6 C_7 - S_6 S_7 C_\alpha) + & S_5 (C_6 S_7 + S_6 C_7 C_\alpha) - & \\ (C_5 S_7 C_8 - S_5 S_6 S_8) S_\alpha - & (C_5 S_7 S_8 + S_5 S_6 C_8) S_\alpha - & S_5 C_7 S_\alpha & d(C_5(C_\alpha - 1) - S_5 S_6 S_\alpha) \\ C_5 S_8 C_\alpha & C_5 C_8 C_\alpha & 0 & 1 \\ 0 & 0 & 0 & \end{bmatrix}, \quad (6.37)$$

where $\alpha = 45^\circ$.

Then, knowing the azimuth and declination of the device, pitch and yaw coordinates could be found as per Equations (2.3) and (2.4).

The roll angle θ_n can be found by substituting (2.5) into

$$S_1(C_2 S_3 + S_2 C_3 C_\alpha) - S_1 C_3 S_\alpha = S_a S_o S_n + C_a C_n \quad (6.38)$$

and

$$S_4(S_2 C_3 + C_2 S_3 C_\alpha) + C_2 C_4 S_\alpha = C_o C_n \quad (6.39)$$

which correspond to elements (2,2) and (3,3) in (2.1), yielding

$$-S_1 S_2 C_2 (1 + C_\alpha) - C_1 C_2 S_\alpha = S_a S_o S_n + C_a C_n \quad (6.40)$$

and

$$S_1 S_2 C_2 (1 + C_\alpha) + C_1 C_2 S_\alpha = C_o C_n. \quad (6.41)$$

Adding (6.40) and (6.41) yields

$$S_a S_o S_n + C_a C_n + C_o C_n = 0 \quad (6.42)$$

which can be transformed into

$$\frac{S_n}{C_n} = -\frac{C_a + C_o}{S_a S_o} \quad (6.43)$$

or

$$\tan(\text{roll}) = -\frac{\cos(\text{pitch}) + \cos(\text{yaw})}{\sin(\text{pitch})\sin(\text{yaw})} \quad (6.44)$$

Equation (6.44) is consistent with the fact that Omni-Wrist III is a two-degree-of-freedom system supporting rotations around the pitch and yaw axes only – rotation around the roll axis is given by the pitch and yaw coordinates.

7. CONCLUSIONS

This report presents a hybrid beam steering system for mobile quantum communication terminals. The proposed system comprises a novel robotic manipulator Omni-Wrist III that provides a wide range of motion, and an acousto-optic Bragg steerer, which assures the low-magnitude agile beam steering in the vicinity of any point on the operational hemisphere. A hierarchical control system was synthesized to maximize the combined effect of these devices and utilize their advantages to the fullest extent. As could be seen from the simulation results, the hybrid steerer enjoys good robustness, while achieving high tracking accuracy over an extended field of view. It was demonstrated that this system facilitates jitter rejection exceeding 10dB over a range of frequencies spanning up to a few kHz.

A number of issues specific to quantum communication using polarization-based encoding, and single-photon transmission were identified. A viable solution to the problem of maintaining polarization of the transmitted signal was developed. It allows to identify rotation of the polarization plane relative to the Earth coordinates due to changing orientation of the entire communication platform, as well as the steering performed by the coarse pointing device (gimbal). If necessary, the issue of polarization change in the process of acousto-optic steering could be addressed in the near future.

It may also be necessary to perform a more detailed simulation study of the tracking system performance in the presence of other environmental effects, such as background radiation, photodetection noises, etc.

REFERENCES

- [1] S.B. Niku, "Introduction to Robotics. Analysis, Systems, Applications," Prentice Hall, 2001.
- [2] J. Sofka, V. Skormin, V. Nikulin, D. Nicholson and M. Rossheim "New Generation of Gimbals Systems for Laser Positioning Applications," *Proc. SPIE, Vol. 5160, p. 182-191, Int. Symposium on Optical Science and Technology*, San Diego, CA, 3-8 Aug. 2003.
- [3] J. Sofka, "Gimbals Control for Aerospace Applications," *MS Thesis*, SUNY at Binghamton, NY, 2002.
- [4] Amnon Yariv, Pochi Yeh, *Optical Waves in Crystals*, John Wiley & Sons, 1984.
- [5] J. Xu, R. Stroud, *Acousto-Optic Devices. Principles, Design and Applications*, John Wiley & Sons, 1992.
- [6] V.A. Skormin, V. Nikulin, M. Bouzoubaa, "Analysis and Characterization of an Acousto-Optic Beam Steering System," *Final Report for NASA Jet Propulsion Laboratory*, Pasadena, Ca, Sept. 2000.
- [7] V. Nikulin, M. Bouzoubaa, V. Skormin, T. Busch, "Modeling of an Acousto-Optic Laser Beam Steering System Intended for Satellite Communication," *Optical Engineering*, Vol. 40, No. 10, Oct. 2001, pp.2208-2214.
- [8] A. Yariv, *Optical Electronics*, CBS College Publishing, 1985.
- [9] Mounir Bouzoubaa, Vladimir Nikulin, Victor Skormin, and Timothy Busch, "Model Reference Control of a Laser Beam Steering System for Laser Communication Applications," *Proc. SPIE, Vol. 4272, pp. 93-103, Free-Space Laser Communication Technologies XIII Conference*, San Jose, CA, 24-25 January 2001.
- [10] H. Seraji, "Decentralized Adaptive Control of Manipulators: Theory, Simulation, and Experimentation," *IEEE Trans. On Robotics and Automation*, Vol. 5, No. 2, April 1989.
- [11] N. E. Wu, V. Nikulin, F. Heimes, and V. Skormin, "A Decentralized Approach to Fault Tolerant Flight Control," *Proc. 4th IFAC Symposium on Safeprocess*, Budapest, Hungary, 14-16 June, 2000.
- [12] J.-J. E. Slotine, W. Li, "Adaptive Manipulator Control: A Case Study," *IEEE Trans. On Automatic Control*, **Vol. 33**, No. 11, November 1988.
- [13] J.-J. E. Slotine, W. Li, "On the Adaptive Control of Robot Manipulators," *The International Journal on Robotics Research*, **Vol. 6**, No. 3, Fall 1987.

- [14] V. Nikulin, J. Sofka, and V. Skormin, "Advanced Lyapunov Control of a Novel Laser Beam Tracking System," *Optical Engineering*, Vol. 44, No. 5, May 2005, pp. 56004-1-8.
- [15] S.-T. Chen and M.R. Chatterjee, "A Numerical Analysis and Expository Interpretation of the Diffraction of Light by Ultrasonic Waves in the Bragg and Raman-Nath Regimes Using Multiple Scattering Theory," *IEEE Trans. On Education*, Vol. 39, No. 1, Feb. 1996.
- [16] M.R. Chatterjee, T.-C. Poon, and D.N. Sitter, "Transfer Function Formalism for Strong Acousto-Optic Bragg Diffraction of Light Beams with Arbitrary Profiles," *Acustica*, Vol. 71, 1990.
- [17] V. Voloshinov, A. Tchernyatin, E. Blomme, and O. Leroy, "A Dozen Bragg Effects in Tellurium Dioxide Single Crystal," *Proc. SPIE*, Vol. 3581, 1998.
- [18] V. Nikulin, V. Skormin, "Genetic Algorithm Optimization for Bragg Cell Design," *Optical Engineering*; Vol. 41, No. 8, Aug. 2002; pp. 1767-1773.
- [19] V. Nikulin, "Fast Acousto-Optic Steering Device for Optical Communication Turrets," *Technical Report for Innovative Technical Solutions*, Nov. 2004.
- [20] J. Sofka, V. Skormin, "Integrated Approach to Electromechanical Design of a Digitally Controlled High Precision Actuator for Aerospace Applications," IEEE International Conference on Control Applications, Munich, Germany, October 2006
- [21] J.L. Marins, X. Yun, E.R. Bachmann, R.B. McGhee, M. J. Zyda, "An Extended Kalman Filter for Quaternion-Based Orientation Estimation Using MARG Sensors," *Proceedings of the 2001 IEEE/RSJ Int. Conf. on Intelligent Robots and Systems*, Maui, Hawaii, 2001
- [22] J.B. Kuipers, *Quaternions and Rotation Sequences: A Primer with Applications to Orbits, Aerospace and Virtual Reality*, Princeton University Press, 1992